Meteoric water and glacial melt in the Southeast Amundsen Sea: A timeseries from 1994-2020

Andrew N. Hennig[1], David A. Mucciarone[2], Stanley S. Jacobs[3], Richard A. Mortlock[4], Robert B. Dunbar[2]

[1]Earth System Science, Stanford University, Stanford, California, 94305, USA
[2]Oceans, Stanford University, Stanford, California, 94305, USA
[3]Lamont-Doherty Earth Observatory, Columbia University, Palisades, New York, 10964, USA
[4]Earth and Planetary Sciences, Rutgers University, Piscataway, New Jersey, 08854, USA

Correspondence to: Andrew N. Hennig (ahennig@stanford.edu)

Abstract. Ice sheet mass loss from Antarctica is greatest in the Amundsen Sea sector, where 'warm' modified Circumpolar Deep Water moves onto the continental shelf and melts and thins the bases of ice shelves hundreds of meters below the sea surface. We use nearly 1000 paired salinity and oxygen isotope analyses of seawater samples collected on seven expeditions from 1994 to 2020 to produce a time series of glacial meltwater inventory for the Southeast Amundsen Sea continental shelf. Water column salinity-$\delta^{18}O$ relationships yield freshwater endmember $\delta^{18}O$ values from -31.3±0.6‰ to -28.4±0.8‰, consistent with the isotopic composition of local glacial ice. Meteoric water inventories, consisting of an estimated >92% glacial meltwater by mass, account for 7.6±0.5 m to 9.2±0.6 m of freshwater in the water column, and exhibit greater interannual variability than trend over the study period, based on the available data.

1 Introduction

Four decades of observations show significant and increasing glacial mass loss from Antarctica (Rignot et al., 2011; Velicogna et al., 2014; Rignot et al., 2019a). A Special Report on the Ocean and Cryosphere in a Changing Climate (SROCC) projected 0.61 m to 1.10 m of sea level rise (SLR) by 2100 under RCP8.5 forcing, with uncertainty largely hinging on the future of the Antarctic ice sheet (IPCC, 2022). Over the past two decades, losses from the West Antarctic Ice Sheet (WAIS) comprised 84±12% of the total Antarctic contribution to SLR (5.5±2.2 mm from 1993-2018; WCRP Global Sea Level Budget Group, 2018), with glaciers flowing into the Amundsen Sea Sector (particularly the Pine Island and Thwaites glaciers) dominating the overall negative mass balance of the ice sheet (Rignot et al., 2019b; Shepherd et al., 2019).

High ice shelf basal melt rates in the Southeast (SE) Amundsen Sea have been linked to the flow of 'warm' and salty modified Circumpolar Deep Water (mCDW) onto the continental shelf, separated by cooler but fresher waters above by a thermocline between 300 m and 700 m (Dutrieux et al., 2014; Jacobs et al., 2011). mCDW flows from the continental shelf break towards SE Amundsen Sea ice

shelves via “central” and “eastern” glacially-carved bathymetric troughs (Nakayama et al., 2013). This ‘warm’ mCDW penetrates into sub-ice shelf cavities (Jacobs et al., 1996; Paolo et al., 2015; Pritchard et al., 2012) where it can access ice shelf grounding lines (Rignot and Jacobs, 2002). To access the Pine Island Ice Shelf (PIIS) grounding line, mCDW passes between the bottom of the ice shelf at ~350 m and a seafloor ridge at ~700 m (Jenkins et al., 2010). Basal melt is driven by total heat transport, dependent more on the thickness of the mCDW layer transported on-shore than its temperature (Dutrieux et al., 2014; Jenkins et al., 2018), with the thickness controlled by local wind forcing of a shelf break undercurrent, in turn influenced by the Amundsen Sea Low. Despite the strong sensitivity of these ice shelves to ocean forcing, and evidence of increasing mass loss in this region, estimates of Antarctic SLR contributions from basal melt remain poorly constrained (van der Linden et al., 2021, 2023).

Southern Ocean water masses have typically have been differentiated and defined by measurements of temperature and salinity, and less often by including oxygen isotopes ($\delta^{18}O$; Jacobs et al., 1985, 2002; Meredith et al., 2008, 2010, 2013; Brown et al., 2014; Randall-Goodwin et al., 2015; Silvano et al., 2018; Biddle et al., 2019). Salinity- $\delta^{18}O$ relationships can be used to infer the source and concentration of highly $\delta^{18}O$-depleted glacial meltwater on seawater properties (Jacobs et al., 1985; Hellmer et al., 1998; Jacobs et al., 2002; Meredith et al., 2008; Randall-Goodwin et al., 2015). A spatial and temporal array of T, S and $\delta^{18}O$ can thus be utilized to track GMW content and distribution, especially in nearshore waters adjacent to melting ice shelves. Prior studies have used $\delta^{18}O$ measurements to estimate meteoric water abundance (precipitation and GMW) in the Amundsen Sea (Biddle et al., 2019; Jeon et al., 2021; Randall-Goodwin et al., 2015) and elsewhere around Antarctica (Meredith et al., 2010, 2018; Silvano et al., 2018) but so far have revealed little about temporal variability or possible trends in GMW content. Here, we use nearly 1000 seawater isotope samples collected during seven austral summers from 1994 to 2020 (**Figure 1**) to investigate meteoric water sources, water column inventories, and their interannual variability in the SE Amundsen Sea.

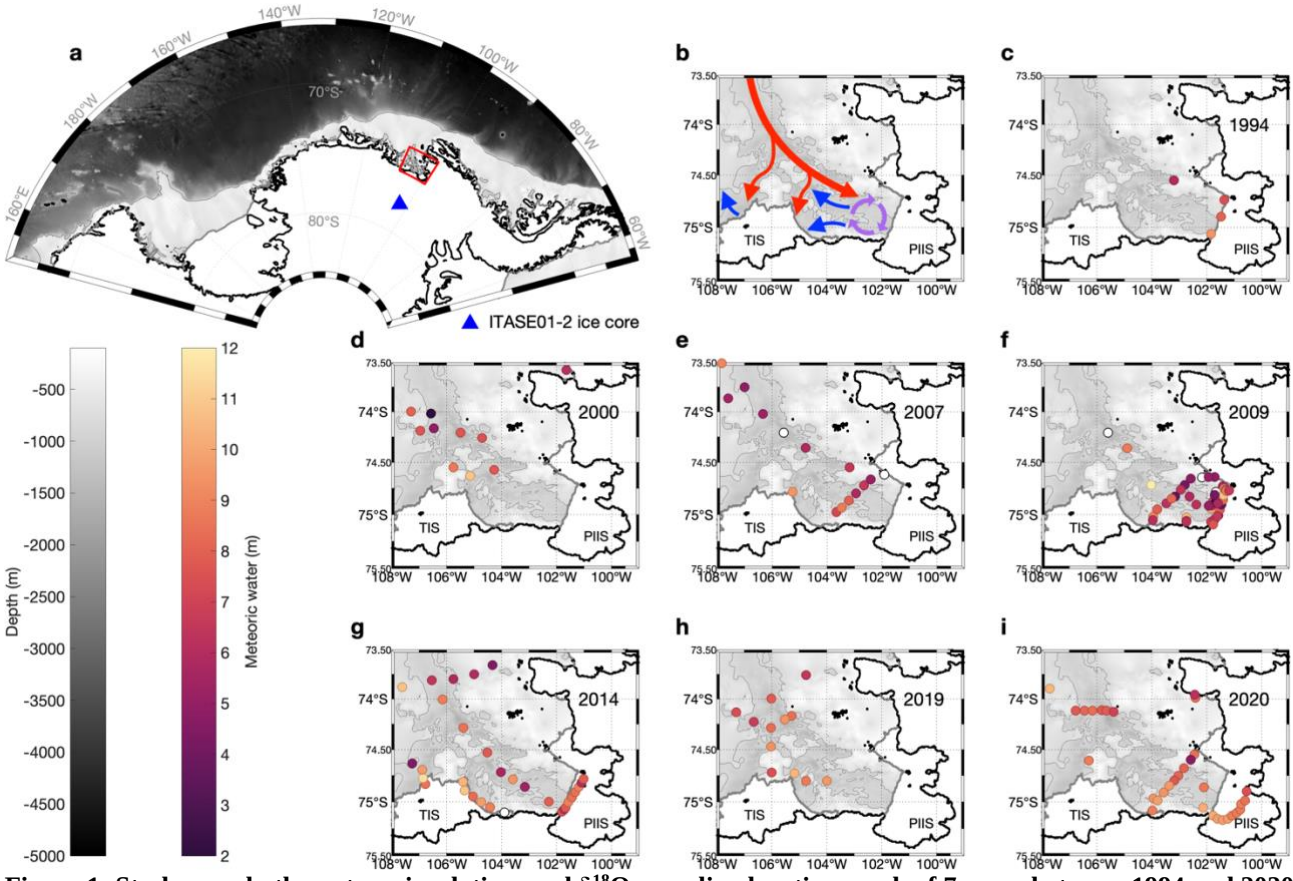

Figure 1: Study area bathymetry, circulation, and $\delta^{18}O$ sampling locations each of 7 years between 1994 and 2020. 800 m isobaths are shown as thin gray lines. (a) SE Amundsen study area, and location of the ITASE01-2 ice core. (b) Location of the Pine Island Bay gyre (purple), pathways of warm deep mCDW (red) toward the ice shelves and pathways of shallower meltwater rich waters (blue) from beneath Pine Island Ice Shelf (PIIS; Nakayama et al., 2019; Wåhlin et al., 2021). (c-i) Colored dots show sample locations, with colors representing vertically integrated glacial meltwater inventories between 0 m and 800 m from 1994 to 2020. Thick gray lines indicate seaward boundaries of Thwaites Ice Shelf (TIS) and the PIIS. Calving fronts are referenced to 2000 (Schaffer et al., 2014; Fretwell et al., 2013), a relatively stable location before a ~20 km retreat following calving events between 2017 and 2020 (Joughin et al., 2021). Stations where sampling did not extend to the seafloor show only partial water column inventories, and stations shown as white dots (2007, 2009, 2014) had only one depth sampled. In 2000, 2007, and 2019, access to sampling along the front of PIIS calving front was precluded by fast ice.

2 Data and Methods

2.1 Sample collection and analysis

We compile data from samples collected during 7 field seasons in the SE Amundsen Sea from 1994 to 2020 (**Figure 1**, **Table 1**). Salinity profiles were obtained using calibrated conductivity cells on SBE911 conductivity-temperature-depth (CTD) instruments, monitored with shipboard bottle sample analyses using Guildline AutoSal and PortaSal salinometers calibrated with IAPSO seawater salinity standards.

In 1994, 2007, 2009 and 2014, $\delta^{18}O$ was measured using an Isotope Ratio Mass Spectrometer (IRMS; Micromass Optima Multiprep or a Finnigan MAT252 HDO). All samples collected in 2019 and 2020, and some in 2007 and 2009, were measured with a Picarro L2140-i Cavity Ring Down System (CRDS). Equivalence has been demonstrated between CRDS and IRMS measurements (Walker et al., 2016; **Appendix A8**). In all cases, values are reported as per mil (‰) deviations(δ), relative to Vienna Standard Mean Ocean Water (VSMOW2; Coplen, 1994).

Table 1: Summary of $\delta^{18}O$ data sources, sampling intervals, methods & applications

Year	Cruise	Sample collection dates	# Samples	$\delta^{18}O$ Technique(s)
1994	NBP94-02 (Hellmer et al., 1998)	14 Mar. 1994 – 15 Mar. 1994	26	IRMS CO_2 equilibration
2000	NBP00-01 (Jacobs et al., 2002)	16 Mar. 2000 – 20 Mar. 2000	62	IRMS CO_2 equilibration
2007	NBP07-02	24 Feb. 2007 – 27 Feb. 2007	74	IRMS CO_2 equilibration, CRDS
2009	NBP09-01	16 Jan. 2009 – 29 Jan. 2009	175	IRMS CO_2 equilibration, CRDS
2014	iSTAR2014 (Biddle et al., 2019)	5 Feb. 2014 – 20 Feb. 2014	213	IRMS CO_2 equilibration
2019	NBP19-01	12 Jan 2019 – 14 Jan 2019	107	CRDS
2020	NBP20-02	5 Feb. 2020 – 8 Mar. 2020	280	CRDS

Some of the 2009 samples were processed at Rutgers University in 2010 using a Micromass IRMS; the remainder in 2020 using a Picarro CRDS system at Stanford University. While the latter samples had not been opened since collection, a substantial number were compromised by evaporation during 11 years of storage. The 2009 samples analyzed in 2020 were scrutinized visually and newly measured sample densities compared with those derived from the CTD measurements. Data from compromised samples were discarded (**Appendix A7**). A subset of 100 samples from 2019 and 2020 were processed concurrently using CO_2 equilibration on a Finnigan MAT252 IRMS and CRDS via vaporizer to ensure data comparability between instrumentation (**Appendix A8**). Measurements for all years achieved a precision of 0.04‰ for IRMS and 0.02‰ for CRDS, based on replicate analyses.

After a review of the literature, we considered a possible salt effect in measured seawater $\delta^{18}O$, as suggested by a small number of studies (Lécuyer et al., 2009; Skrzypek and Ford, 2014; Benetti et al., 2017). As no salt effect offset was applied to the previously published data in this study (1994, 2000, 2014) we have not applied any offset to data from other years. The mCDW $\delta^{18}O$ value (**Table 2**) for 2014 is significantly higher than other years (**Appendix A2**) – likely due to a calibration offset but may also point to sample storage issues. The mCDW and meteoric water endmembers are defined from observations each year, minimizing the impact of interlaboratory offsets on the results (**Appendix A2, Data and Methods 2.2**).

2.2 Three-endmember mixing model

We adapt an approach from Östlund & Hut (1984) as applied in the Peninsula-Bellingshausen-Amundsen region of West Antarctica (Biddle et al., 2019; Jeon et al., 2021; Randall-Goodwin et al., 2015; Meredith et al., 2010) and near the Totten Ice Shelf (Silvano et al., 2018). We use a 3-endmember mixing model (**Equations 1-3**) to determine water source fractions in the field area. The model assumes the observed $\delta^{18}O$ and salinity values result from mixtures of mCDW, sea ice melting/freezing, and meteoric waters contributing a range of $\delta^{18}O$ and salinity signatures. Meteoric waters deeper than 200 m are dominated by ice shelf basal melt, as are surface waters near the ice shelves. Shallower depths in the water column, can also include ice front/wall melt, and iceberg melting. Near-surface waters are also influenced by sea ice melt and formation, and are likely to contain both local and advected sea level precipitation.

Equations 1-3: Three-endmember mixing model. The 3-endmember mixing model uses the absolute salinity and $\delta^{18}O$ of mCDW, sea ice melt, and meteoric water endpoints to solve for the relative fractions of the three water sources in each sample analyzed.

$$f_{sim} + f_{met} + f_{mcdw} = 1 \quad (1)$$

$$f_{sim} * S_{sim} + f_{met} * S_{met} + f_{mcdw} * S_{mcdw} = S_{obs} \quad (2)$$

$$f_{sim} * \delta_{sim} + f_{met} * \delta_{met} + f_{mcdw} * \delta_{mcdw} = \delta_{obs} \quad (3)$$

f = fraction of water source
S = salinity
δ= $\delta^{18}O$
sim = sea ice melt
met = meteoric water
mcdw = modified circumpolar deep water
obs = observed sample

The primary fraction of interest is the meteoric water fraction comprised of ice shelf melt. The meteoric water endmember is defined as the zero-salinity $\delta^{18}O$ intercept of data below 200 m (**Figure 2**). This intercept reflects the average $\delta^{18}O$ of pure meteoric freshwater in the form of ice shelf basal melt (**Results 3.1**, **Appendix A1**). Below 200 m the $\delta^{18}O$-salinity plots yield mixing lines with mCDW as the saltiest, least-depleted component, and meteoric water as the most highly depleted freshwater endmember, indicative of basal meltwater. To minimize issues that could arise from inter-laboratory calibration offsets (**Data and Methods 2.1, Appendix A2**), we define individual mCDW and meteoric water endmembers separately for each year (**Table 2**). Model outputs (mCDW, meteoric water, and sea ice melt fractions) critically depend on appropriate endmember inputs, which will affect resulting water source fractions and trends.

The mCDW is the warmest, saltiest, and least $\delta^{18}O$-depleted water mass in the region and comprises the vast majority of the overall water column. Interannual changes in mCDW inflow will result from variable wind forcing (Dotto et al., 2019; Holland et al., 2019; Kim et al., 2021), combined with on-shelf lateral and vertical mixing. In the 3-endmember mixing model, mCDW and meteoric waters are

defined by the mixing line of data >200m; with mCDW the $\delta^{18}O$ value at the salinity maximum (Biddle et al., 2017) and meteoric water the zero-salinity intercept on the mixing line (**Results 3.1**; **Figure 2**). Sea ice endmember isotopic values adopted from previous studies in the Amundsen and Bellingshausen region (Meredith et al., 2008, 2010, 2013; Randall-Goodwin et al., 2015; Biddle et al., 2019) are based on the $\delta^{18}O$ of surface water with an offset to account for isotopic fractionation due to freezing.

Table 2: Salinity and $\delta^{18}O$ values used in the 3-endmember mixing model. mCDW and meteoric components are defined independently using the mCDW-GMW mixing line produced from (>200 m depth) salinity and $\delta^{18}O$ observations for each year, as the salinity maximum and zero-salinity intercept, respectively (**Results 3.1; Figure 2; Appendix A1**). Sea ice melt uses single values for each year. Salinities are reported as absolute salinity (g/kg).

Year	mCDW salinity (g/kg)	mCDW $\delta^{18}O$ (‰)	Meteoric water (GMW) $\delta^{18}O$ (‰)	Sea ice melt salinity (g/kg)	Sea ice melt $\delta^{18}O$ (‰)
1994	34.86±0.010	-0.01±0.01	-29.4±1.4		
2000	34.86±0.011	-0.05±0.01	-28.7±0.6		
2007	34.89±0.009	-0.02±0.02	-28.4±0.8		
2009	34.87±0.002	0.01±0.02	-29.1±0.6	7	2.1
2014	34.85±0.015	0.08±0.01	-31.3±0.5		
2019	34.88±0.006	-0.09±0.01	-30.0±0.4		
2020	34.87±0.017	-0.10±0.01	-29.1±0.2		

3 Results

3.1 Meteoric waters defined by the $\delta^{18}O$ – salinity relationship

Freshwater endmembers (zero-salinity $\delta^{18}O$ intercepts) over the seven sampled summers differ by <3‰, ranging from -28.4‰ to -31.3‰ with a standard deviation of 1.0‰ (**Figure 2**, **Table 2**). These measurements are consistent with the nearest ice-core (ITASE01-2, from 77.84°S, 102.91°W, **Figure 1a**; Schneider et al., 2006; Steig et al., 2005) with a mass-averaged $\delta^{18}O$ value of -29.8±1.9‰. Ice cores further east have less negative $\delta^{18}O$ values (~-20‰; Thomas et al., 2009), while those further west are more negative (~-40‰; Blunier & Brook, 2001). Intercept uncertainty from analytical precision and environmental variability (**Appendix A3**) ranges from ±0.2‰ in 2020 to ±1.4‰ in 1994, varying inversely with the number of data points available.

Local precipitation, in the form of snow collected in early 2019 at 72.5°S, yielded a $\delta^{18}O$ value of ~-15‰, consistent with previous observations and model outputs at sea-level from that latitude (Masson-Delmotte et al., 2008). Endmember extrapolations from the regional salinity and $\delta^{18}O$ measurements indicate that freshwater added to the water column is dominated by locally derived GMW, as intimated earlier from 1994 data (Hellmer et al., 1998).

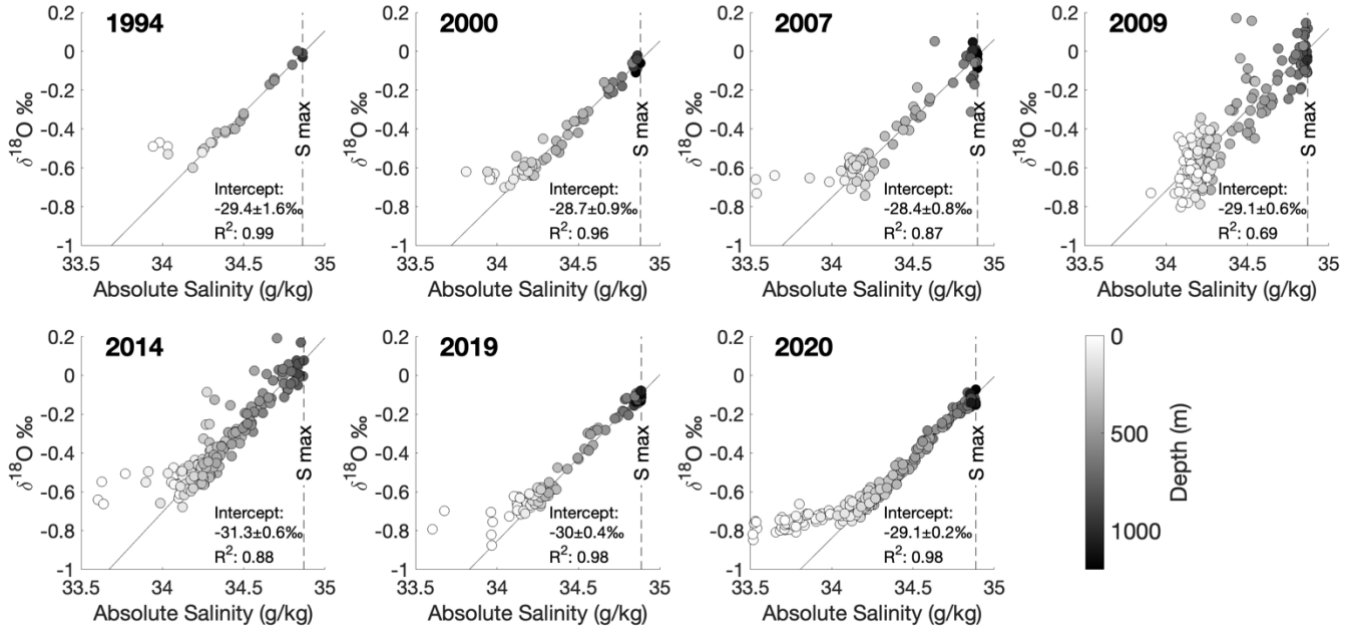

Figure 2: Salinity vs $\delta^{18}O$ plots for each year, shaded by depth. Linear regressions (solid) gray lines (with R^2 from 0.69 in 2009 to 0.99 in 1994) project to zero-salinity glacial meltwater endmember intercepts using data >200m. Dashed vertical lines indicate the mCDW salinity maxima (**Table 2**). Data diverge from the mCDW-meteoric water mixing line in the upper water column, where sea ice melt freshens the resultant mixture but has an enriching effect on $\delta^{18}O$ (**Table 2**). Years with greater divergence at the surface have more sea ice melt (**Appendix A6**). The most negative upper water column seawater $\delta^{18}O$ measurements tend to reach minima between -0.9‰ and -0.6‰.

Samples below 200 m show a strong $\delta^{18}O$-salinity relationship, forming a mixing line between mCDW and a (glacial) meteoric freshwater endmember introduced at depth. Closer to the surface (from 10 m in 2009 to 160 m in 2000) data diverge from the mixing line due to the net influence of sea ice melt and local precipitation, moving the $\delta^{18}O$ of the mixture in a more positive direction. Below 200m the $\delta^{18}O$-salinity relationship is strongly linear; greater scatter in 2009 and 2014 likely results from sample storage issues (**Appendix A7**).

In 2009 and 2014, samples were collected in bottles with taped (2009) or parafilm-wrapped (2014), threaded caps, and stored for several years before analysis. Samples from 2019 and 2020 were collected in glass serum vials capped with rubber stoppers and aluminum seals (**Appendix A9**), which internal lab data demonstrate the maintenance of seawater $\delta^{18}O$ sample integrity for 5+ years. Scatter occurs mostly in the positive $\delta^{18}O$ direction (particularly in 2014), indicative of sample evaporation.

3.2 Vertical distribution of meteoric water illustrates basal melt

A 3-endmember mixing model of mCDW, sea ice melt, and meteoric water is used to determine the constituent freshwater components of seawater (**Equations 1-3**) at all depths sampled in the water column (**Figure 3**). By using mCDW and meteoric water endmember values based on data from each

year individually, minimizing the potential impact of analytical calibration offsets between laboratories on the calculated meteoric water fractions. (**Data and Methods 2.1**; **Appendix A2**).

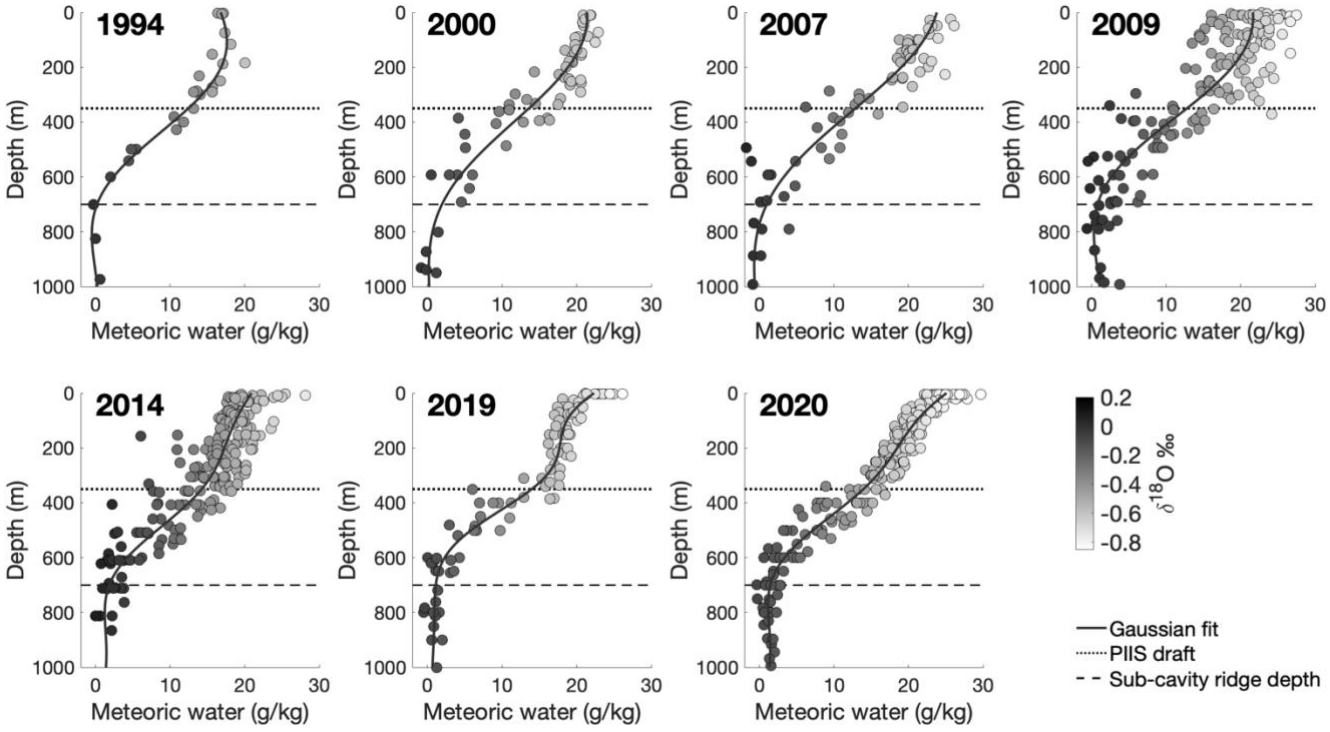

Figure 3: Meteoric water fractions (g/kg) vs depth. Shading shows $\delta^{18}O$ value, and solid lines represent Gaussian Process regression fits. Dotted and dashed lines show the depth of the PIIS draft and sub-cavity ridge (Jenkins et al., 2010). Slightly negative meteoric water values at depth occur when the sample exceeds the mCDW endmember value (**Table 2; Data and Methods 2.2**), the result of environmental, sampling and analytical uncertainties (discussed in further detail in **Results 3.4**).

Evidence of highly $\delta^{18}O$-depleted freshwater is found at depths above ~700 m (the depth of PIIS sub-ice shelf ridge; Jenkins et al., 2010), with highest concentrations found at depths shallower than 350 m – above which glacial meltwater has been observed to flow out from beneath the ice shelf (Biddle et al., 2017; Naveira Garabato et al., 2017). Made less dense by the addition of GMW, such outflows rise through denser waters above, along ice shelf calving fronts and strongly influencing surface waters in this region (Dierssen et al., 2002; Mankoff et al., 2012; Thurnherr et al., 2014; Fogwill et al., 2015).

Sea ice melt and mCDW fractions are discussed in **Appendix A6**.

3.3 Average meteoric water inventory over the last two decades

Average meteoric water column inventories (**Table 3**) in the study area were estimated by depth integrating the Gaussian Process fit of the calculated meteoric water fractions (solid lines in **Figure 3**). The average meteoric water column inventory was relatively low in 1994 and higher from 2000-2020.

Strongly influenced by the low meteoric water inventory in 1994, a linear regression of the mean meteoric water inventories suggests an increase of 0.03±0.02 m/y (p-value 0.28). Meteoric water column inventories have uncertainties of <0.8 m, based on analytical precision and environmental variability of the model inputs (**Results 3.4**). Assuming 1 m water equivalent (2 years) of precipitation (Boisvert et al., 2020; Donat-Magnin et al., 2021), the meteoric water inventories are likely to consist of >92% GMW (**Appendix A5**).

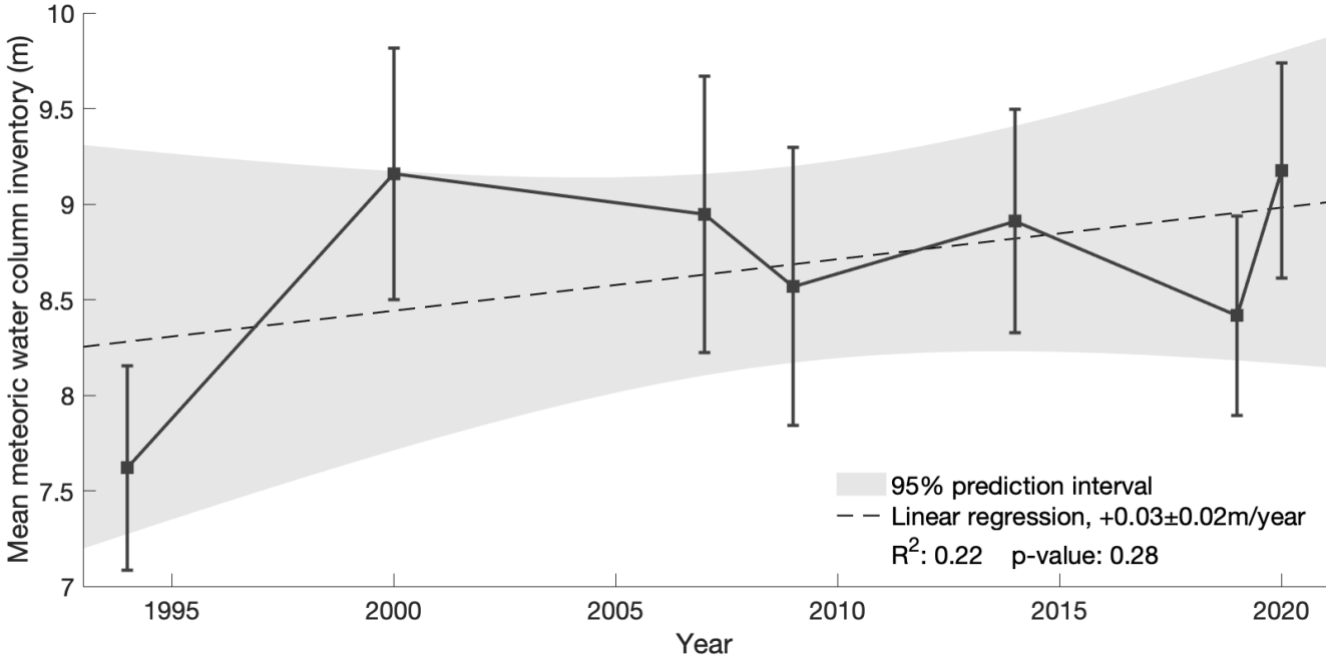

Figure 4: Average meteoric water column inventory. Depth-integrated meteoric water content from the Gaussian Process fit (**Figure 3**) between the sea surface and 800 m. Error bars show the uncertainty (**Table 3**) associated with data volume, analytical precision, and uncertainty in endmember values (**Data and Methods 2.2**). A linear regression of the mean values shows an increase of 0.03±0.02 m/year (p-value 0.28)**.** Grey shading shows the 95% prediction interval for the linear regression.

3.4 Uncertainty and sensitivity analyses

3.4.1 Analytical precision and environmental variability

We ran 10,000 Monte Carlo simulations where observations were perturbed around their measured value by uncertainty associated with analytical precision (0.04‰ $\delta^{18}O$ for IRMS; 0.02‰ $\delta^{18}O$ for CRDS; 0.002 g/kg salinity) and water source endpoints (mCDW, sea ice melt, meteoric water). mCDW and meteoric water endpoints were defined using perturbed observational data for each simulation, and around the selected endpoint by uncertainty associated with environmental variability (**Table 3, Appendix A3**). Uncertainty in mean meteoric water fractions ranges from 1.1 g/kg in 2019 to 1.7 g/kg in 2007/2009, and uncertainty in mean meteoric column inventories ranges from 6-9%.

Calculated water fractions are most strongly influenced by changes made to the mCDW endmember (comprising ~99% of an 800m water column on average; ~95% in surface waters rich in meteoric water and sea ice melt). Meteoric water fractions vary inversely with the magnitude of the meteoric water endmember $\delta^{18}O$. 1994 has the fewest samples, but the strongest fit (**Figure 2**), and exhibits similar uncertainty to other years (**Figure 4**).

Table 3: Meteoric water column inventory analytical and environmental uncertainty. Depth-integrated meteoric water content using the Gaussian Process fit (Figure 3) between the sea surface and 800 m depth. Uncertainties are associated with number of data points, analytical precision, and environmental variability in endmember values (**Data and Methods 2.2**).

Year	Meteoric water fraction uncertainty (g/kg)	Meteoric water column inventory (m)	% meteoric water column inventory uncertainty
1994	1.5	7.6±0.5	7.0%
2000	1.7	9.2±0.7	7.2%
2007	1.7	8.9±0.7	8.1%
2009	1.7	8.6±0.7	8.5%
2014	1.5	8.9±0.6	6.6%
2019	1.1	8.4±0.5	6.1%
2020	1.2	9.2±0.6	6.1%

3.4.2 Spatial variability

This study relied on the compilation of data collected for 6 independent studies over 7 different cruises. To determine the impact of inconsistency in sampling locations each year, two different spatial sensitivity analyses were used. First, we conducted 10,000 simulations, for each year selecting random sets of 3 stations within the field area. In each case, mCDW and meteoric water endmembers, and mean meteoric water column inventories were calculated using only those data. Uncertainty is represented as the standard deviation of those results (**Table 4**).

Table 4: Results of randomized spatial sensitivity analysis. Uncertainty is represented by the standard deviation of the results of 10,000 simulations for each year, calculating results using data from only 3 randomly selected stations.

Year	mCDW absolute salinity (g/kg)	mCDW $\delta^{18}O$ (‰ vs VSMOW)	mCDW potential temperature (°C)	Meteoric water $\delta^{18}O$ (‰ vs VSMOW)	Average meteoric water column inventory (m)	Meteoric water fraction uncertainty (g/kg)
1994*	34.86±0	-0.01±0.01	1.08±0.01	-29.4±0.6	7.6±0.2	0.1
2000	34.86±0.012	-0.06±0.02	1.03±0.07	-28.7±1.6	8.8±0.5	0.8
2007	34.89±0.009	-0.03±0.04	1.18±0.03	-27.8±3.4	9.0±0.7	1.1
2009	34.87±0.002	-0.01±0.06	1.17±0.01	-28.9±4.1	8.8±0.7	1.8
2014	34.85±0.015	0.05±0.03	1.10±0.04	-31.2±3.3	8.5±0.8	1.1
2019	34.88±0.006	-0.10±0.01	1.08±0.06	-29.6±1.6	8.5±0.4	0.6
2020	34.87±0.017	-0.12±0.02	1.03±0.01	-29.0±1.4	8.8±0.6	0.7

* As 1994 has only 4 sampling locations, and the strongest fit of any year **(Figure 2)** its uncertainty may be artificially decreased

Additionally, we conducted a spatial sensitivity analysis by separately analyzing different spatial groups of stations across each year (**Figure 5, Table 5**), running 10,000 Monte Carlo analyses for each group as described in **Results 3.4.1**. Uncertainty is represented as the standard deviation of those results (**Table 5, Table A2**).

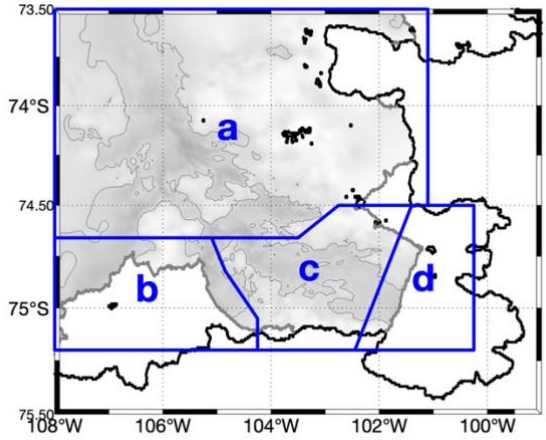

Figure 5:Boundaries of geographic groupings used for spatial sensitivity analysis. Blue lines show boundaries of geographic areas analyzed separately. Gray shading shows bathymetry, with isobaths drawn at 800m. More detailed maps for each year are in Appendix A4.1.

Table 5: Summarized results of meteoric water column inventory (m) from spatial sensitivity analysis (Figure 5). Results by year in rows, and by area group in columns. See Appendix A4.1 for further detail.

	a	b	c	d
1994	6.3±0.5*	-	-	8.0±0.6
2000	9.2±0.7	-	-	-
2007	8.4±0.8	10.3±0.8*	9.0±0.7	-
2009	7.0±0.6*	-	8.7±0.8	8.5±0.7
2014	8.3±0.6	10.1±0.7	7.9±0.5	7.5±0.5
2019	8.2±0.6	10.0±0.7	8.2±0.5	-
2020	8.7±0.6	-	8.7±0.5	8.5±0.5

* Data from only one station. For 1994, 2007, and 2009, result is based on only 8, 4, and 4 samples, respectively.

Both sets of spatial sensitivity analyses show little spatial variability in calculated endmember values or mean meteoric water column inventories, possibly excepting 2009, where there are known sample quality concerns. Mean meteoric water column inventories are remarkably consistent spatially, except those calculated from stations in Group b alongside the TIS, which showed significantly higher meteoric water inventories than the rest of the study area. Although only 1 and 2 stations alongside the TIS were sampled in 2007 and 2019, the average column inventories are consistent with the 2014 data, where there were 8 stations in Group b. The higher inventories in Group b are suggestive of an accumulation of basal melt, and consistent with findings from another study showing that basal melt from beneath PIIS ends up along the eastern edge of TIS (Wåhlin et al., 2021). The relative insensitivity of sampling location (except for those alongside TIS) in calculated mean meteoric water column inventories suggests that precise reoccupation may be unnecessary, and potentially that a relatively

small number of stations/samples could be used to reliably assess mean meteoric water column inventory in this region.

4 Discussion

4.1 The utility of zero-salinity $\delta^{18}O$ intercepts

The meteoric water endmember has been described as the least well-constrained component (Meredith et al., 2008, 2010, 2013; Randall-Goodwin et al., 2015; Biddle et al., 2019) of the three-endmember mixing model employed here, leading previous studies to use plausible mean meteoric $\delta^{18}O$ values, falling between the $\delta^{18}O$ value of glacial melt and local precipitation. However, $\delta^{18}O$-salinity plots presented here (**Figure 2**) show mixing diagrams of different water sources in the SE Amundsen Sea and suggest that the meteoric endmember for waters below the surface mixed layer can be well-constrained. mCDW is the saltiest, and least-depleted water, while glacial meltwater is fresh and the most depleted in $\delta^{18}O$. Data from deeper than 200 m fall along a mixing line between mCDW and a meteoric freshwater source with a $\delta^{18}O$ value indicative of local glacial freshwater (Steig et al., 2005; Schneider et al., 2006), with lower uncertainty than the mass-weighted standard deviation of the average $\delta^{18}O$ of the ITASE01-2 ice core (**Figure 2**).

The 2014 data here was previously used in another study (Biddle et al., 2019), where they selected -25‰ as a meteoric water $\delta^{18}O$ endmember. In comparison to the meteoric endmember used in this study (-31.3‰ for 2014), a -25‰ endmember results in overestimating mean (800 m water column) meteoric water content by 2 m (23%), and underestimating mean sea ice melt by 2.9 m – changing the signal from one of net sea ice melt (this study) to one of net formation (Biddle et al., 2019). The -25‰ endmember was selected as a "mean" meteoric water endmember midway between the $\delta^{18}O$ of GMW and precipitation as defined in another study (Randall-Goodwin et al., 2015). We estimate that >92% of the meteoric water in the study area is GMW (**Discussion 4.2**, **Appendix A5).** Determining the meteoric water endmember using the better-constrained zero-salinity $\delta^{18}O$ intercept of the sample data mixing line (**Data and Methods 2.2**) provides more accurate meteoric water and sea ice melt fractions. The length of the intercept extrapolation emphasizes the importance of careful sample collection, storage, and high-precision analyses.

4.2 Basal meltwater and precipitation

Precipitation grows increasingly depleted in ^{18}O with latitude (Dansgaard, 1964; Gat and Gonfiantini, 1981; Ingraham, 1998; Masson-Delmotte et al., 2008) and altitude (Dansgaard, 1964; Friedman and Smith, 1970; Siegenthaler and Oeschger, 1980; Ingraham, 1998; Araguás-Araguás et al., 2000; Sato and Nakamura, 2005; Masson-Delmotte et al., 2008). Most (88%) of spatial variation in the $\delta^{18}O$ of Antarctic precipitation can be explained by linear relationships between latitude, elevation, and distance from the coast, with elevation being the primary driver (Masson-Delmotte et al., 2008). Precipitation collected during the NBP19-01 cruise in the study had a $\delta^{18}O$ value of -15‰, consistent with other data from that latitude and elevation (Gat and Gonfiantini, 1981; Ingraham, 1998; Noone and Simmonds,

2002; Masson-Delmotte et al., 2008). Precipitation collected at Halley Bay (75.58°S, 20.56°W, 30m elevation) has an average composition of -22.0±5.6‰, while that collected at Rothera Point (67.57°S, 68.13°W, 5m elevation) has an average composition of -13.5±3.4‰, and precipitation collected at Vernadsky (65.08°S, 63.98W, 20m elevation) has an average composition of -10.2±3.0‰ (Global Network of Isotopes in Precipitation (GNIP), 2023).

The nearest Ice cores to our site (ITASE01-2, Steig et al., 2005; Schneider et al., 2006; Siple, Mosley-Thompson et al., 1990) have average $\delta^{18}O$ compositions of -29.6±1.6‰. Using locally collected salinity and $\delta^{18}O$ data from deeper than 200 m to calculate a zero-salinity intercept, we identify average freshwater endmembers ranging from -31.3±0.8‰ to -28.4±0.8‰ (average 29.3±0.7‰). The similar zero-salinity intercept, and strong linear salinity- $\delta^{18}O$ relationship below 200 m demonstrates that glacial freshwater is responsible for the observed freshening signal. We find roughly half of the total meltwater inventory in the upper 200 m, below which inventories yield the same general trend in interannual variability (**Appendix A5).** This indicates the observed variability results from changes in glacial meltwater content, and not from interannual variability in local precipitation.

The Pine Island/Thwaites area receives ~0.5 m/y (water equivalent) of precipitation (Donat-Magnin et al., 2021), and the residence time of deep shelf waters here is ~2 years (Tamsitt et al., 2021). We recalculated our meteoric water column inventories assuming 2 years' worth of local precipitation ($\delta^{18}O$ -15‰) in the upper 200 m, and find that on average, the addition of precipitation decreases the meteoric water ($\delta^{18}O$ ~-30‰, **Table 2**) content by 0.55±0.01 m, and increases sea ice melt by 0.57±0.03 m, indicating that >92% of the meteoric water column inventory consists of GMW (**Appendix A5**). A substantial fraction of local (and non-local) precipitation will be deposited on sea-ice, much of which is subsequently advected out of the study area (Assmann et al., 2005), and as a result have no impact on locally measured meteoric water content, suggesting that GMW could comprise an even greater fraction.

While previous studies (Biddle et al., 2019; Meredith et al., 2010) have excluded the upper water column from GMW accounting, due to uncertainty surrounding the impact of local precipitation, our results suggest realistic (glacial) meteoric water content can still be estimated in the upper water column. Nearly half (~4 m) of the water column meteoric water content resides in the upper 200 m, and >92% of water column meteoric water is comprised of glacial meltwater (**Appendix A5**). Discounting this upper water column meteoric water unnecessarily hampers the usage of this technique for glacial meltwater accounting. The potential for overestimating (glacial) meteoric water due to precipitation is dwarfed by the potential for underestimating glacial meltwater content by excluding the upper water column.

4.3 Temporal changes in mean meteoric water column inventories

We have estimate average meteoric water column inventories in the SE Amundsen Sea using seawater oxygen isotopes and salinity in a three-endmember mixing model. In 1994, 2007, 2014, and 2020, there

is a tendency for the maximum integrated meteoric water volume to extend westward from the SW corner of the PIIS, and along the eastern TIS (**Figure 1**), consistent with the gyre-like circulation there (Thurnherr et al., 2014). This pattern of meteoric water distribution is consistent with local GMW patterns previously observed using traditional hydrographic tracers (Thurnherr et al., 2014; Naveira Garabato et al., 2017; Wåhlin et al., 2021).

Local meteoric water content varies from a low of 7.6±0.5m in 1994 to highs of 9.2±0.6m in 2000 and 2020. Inventories fluctuated over the latter period, without apparent trend, dependent on the spatial and temporal coverage of available datasets. While salinity and $\delta^{18}O$ alone cannot be used to determine basal melt rates, the average meteoric water inventories are sufficient to identify relatively small changes in melt rates, assuming a constant residence time. The inventories are consistent with other studies suggesting relative stability in recent decade-scale glacial melt rates with significant interannual variability (Paolo et al., 2018; Dotto et al., 2019; Adusumilli et al., 2020; Flexas et al., 2022). A recent modelling study shows an increase in basal melt through the 1990s, followed by relative stability from 2000-2020 (Flexas et al., 2022).

The mCDW entering the SE Amundsen Sea and accessing the underside of the ice shelves has been shown to exhibit little seasonal variability, with a maximum variance in T of <0.1°C, salinity of <0.05 g/kg, and thickness of <50 m (Mallett et al., 2018). All samples used in this study were collected from 12 January to 15 March, while melt rates for the PIIS and TIS exhibit very little seasonal variability (Kimura et al., 2017). With a residence time of ~2 years (Tamsitt et al., 2021), it is unlikely that the variability in yearly meteoric water column inventories is a product of a seasonal signal.

Glacial meltwater measured in the SE Amundsen Sea includes mCDW-driven basal melt, local iceberg melt, and meltwater entering the ocean at the grounding zone that is driven by the geothermal heat flux to the base of the ice sheet (~5.3 Gt/y; Joughin et al., 2009). The greatest uncertainty in using average meteoric water inventories as a means for GMW accounting arises from the poorly constrained residence time of regional shelf waters, as there has been little study of this component. With local circulation generally moving waters westward (Nakayama et al., 2013; Thurnherr et al., 2014; Naveira Garabato et al., 2017; Nakayama et al., 2019; Wåhlin et al., 2021), it is likely that the calculated meteoric water fractions in the study area (with the exception of those on the western side of TIS) are primarily comprised of basal melt from PIIS.

Assuming a mean residence time of 2 years (Tamsitt et al., 2021) and GMW comprising >92% of total meteoric water column content (**Appendix A5**) is representative of the whole study area (~30,000 km^2 ocean), we estimate GMW inputs of between 106±17 Gt/y in 1994 to 129±17 Gt/y in 2000/2020. Though empirical, these figures are consistent with satellite-based estimates of mass loss from PIIS via basal melt (Rignot et al., 2013, 2019a), demonstrating the utility of geochemical ocean measurements for estimating ice shelf melt rates.

5 Conclusion

We use seawater $\delta^{18}O$ and salinity data collected in the SE Amundsen Sea from 1994 to 2020, to calculate inventories of meteoric (fresh) water through the water column. Freshwater intercepts from $\delta^{18}O$-salinity plots produce a well-constrained meteoric water endmember consistent with measurements from regional ice cores, and indicative of glacial meltwater. While limited by sampling years and number of observations, meteoric water (which we estimate to be >92% GMW) measured in 1994 is lower than measurements made from 2000-2020, where meteoric water content averaged 8.9±0.3m, with a maximum difference of 0.75m. These results are consistent with recent studies showing an increase in basal melt through the 1990s, followed by relative stability and interannual variability from 2000 through 2020. A linear increase of 0.03±0.02 m/y over the study period is insignificant, with interannual variability that is larger than the increasing trend in meteoric water content.

The WAIS is an important region for understanding sea level rise, as changes in winds and ocean circulation can increase basal melting of ice shelves, and the flow of their ice streams into the sea. Changes in meteoric water inventories in the SE Amundsen Sea study region are consistent with satellite-based estimates of annual mass loss from the PIIS. These results demonstrate the utility of seawater $\delta^{18}O$ and salinity data as an independent method for estimating ice shelf basal melt rates. Regular sampling for $\delta^{18}O$ and salinity in this region could reveal if the existing record and its variability will extend into an era when ice shelves are likely to be thinner, with their grounding lines deeper and farther south. Integration of $\delta^{18}O$ data into numerical models could also further our understanding of ocean circulation and ice loss along this climatically sensitive sector of the WAIS.

APPENDIX

A1 Defining mCDW

Modified Circumpolar Deep Water (mCDW) is one of three endmember waters we use in a mixing model to determine glacial meltwater fractions. As the salinity and $\delta^{18}O$ of mCDW are well observationally well constrained, with interannual variability and properties that are defined separately for each year, as in **Figure A1** with 2020 data. Being the warmest, saltiest water on the continental shelf, mCDW appears at the top-right on a T-S diagram (Panel a), where it also identifies waters that are the least-depleted in $\delta^{18}O$.

In Panels b and c, the same 2020 data show the keystone positions of mCDW in temperature/salinity/$\delta^{18}O$/depth space. The red and blue dashed lines show property mixing lines between mCDW, glacial meltwater (GMW) and sea ice melt, with the colder waters being fresher and more depleted in $\delta^{18}O$. Most data are above ~800 m, with the least $\delta^{18}O$ depletion in a few deep depressions. Waters that fall off the mCDW-GMW mixing line in the upper 200m have been influenced by sea ice melting/formation and atmospheric processes. Sea ice melt has a slightly positive (+2.1‰) $\delta^{18}O$, while GMW has a very negative (~-30‰) $\delta^{18}O$. Both freshen seawater, with the sea ice melt slightly counterbalancing the strong negative $\delta^{18}O$ of GMW.

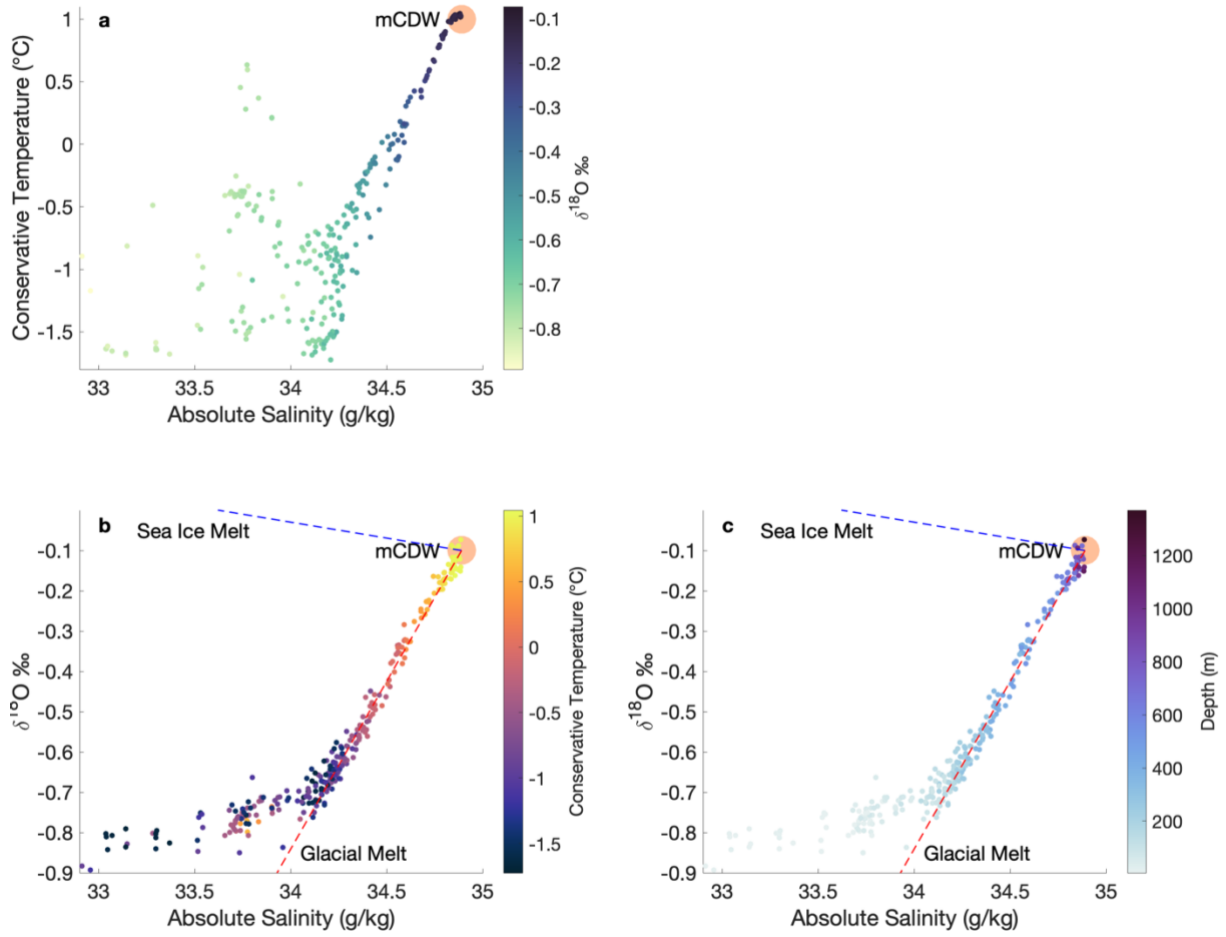

Figure A1: Temperature, salinity, and $\delta^{18}O$ and depth from 2020 data. A) T-S diagram with colorbar showing $\delta^{18}O$. b) $\delta^{18}O$ vs salinity with colorbar showing temperature. C) $\delta^{18}O$ vs salinity with colorbar showing sample depth. Data diverge from the mCDW-glacial melt mixing line at depths shallower than 200 m due to the presence of sea ice melt in the admixture. In Panels b and c, dashed lines show the associated property mixing lines for mCDW mixing with sea ice melt, or GMW.

In **Figure 2** of the main text, $\delta^{18}O$-salinity plots for each year reveal several data points near the salinity maximum, with some variability in the corresponding $\delta^{18}O$. Below 200 m, trendlines extrapolated to zero-salinity intercepts define the mCDW and meteoric water (GMW) endmemebers used in the mixing model. mCDW and meteoric water $\delta^{18}O$ are defined at the salinity maximum and zero-salinity intercepts of the trendlines (**Table 2**). The mCDW location corresponds to conventional measures of the deepest and warmest waters on the continental shelf. The calculated zero-salinity intercept values are consistent with the properties of locally available GMW.

A2 Inter-laboratory offsets

$\delta^{18}O$ data from different laboratories are subject to possible systematic offsets. For example, a ~0.1‰ $\delta^{18}O$ offset between the 2014 data and other years (**Figure A2**) is likely the result of an inter-laboratory calibration offset. On the other hand, greater scatter in the 2009 data suggests that evaporation during sample storage left some samples less depleted in $\delta^{18}O$. Here, we primarily compare calculated meteoric water fractions rather than $\delta^{18}O$ values, with mCDW and meteoric water signatures defined separately for each year so that any offset will not affect the values of samples from that year relative to their mCDW/meteoric water signatures.

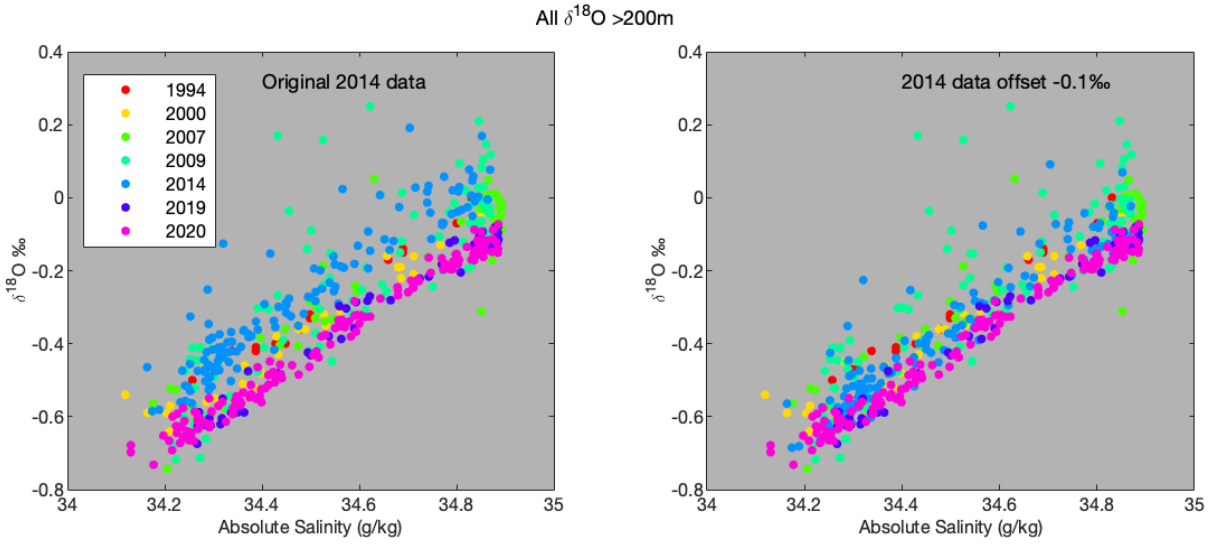

Figure A2: $\delta^{18}O$ vs Absolute salinity for all years, from data >200 m. Left panel: All $\delta^{18}O$ vs salinity data, with the 2014 data as published in (Biddle et al., 2019). Right panel: same, with a -0.1‰ offset correction applied to the 2014 data.

A sensitivity analysis, all sample data from a given year were offset, and mCDW/meteoric water signatures re-calculated using the offset data. The result and endmembers were used to calculate meteoric water fractions in the 3-endmember mixing model, with sea ice melt values remaining static. We found that an offset of 5.7‰ $\delta^{18}O$ (**Figure A3**) would be necessary to change the calculated meteoric water fraction by an amount greater than the analytical precision (±0.04‰ $\delta^{18}O$, ±0.003 g/kg for salinity) and environmental uncertainty based on ice core measurements (±1.9‰ for $\delta^{18}O$) and year-to-year variability in mCDW values (±0.06‰ $\delta^{18}O$). Inter-lab offsets should be less than 0.1‰ (Walker et al., 2016), so any offsets will not be significant when comparing calculated meteoric water fractions.

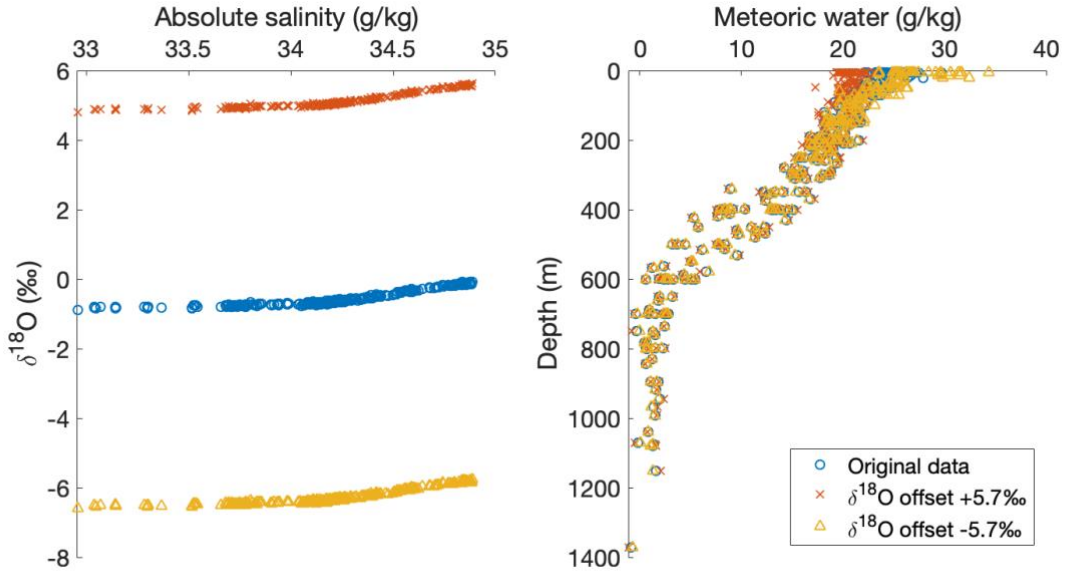

480 **Figure A3: Impact on inter-lab offsets on calculated meteoric (glacial melt) water fraction for NBP20-02 data.** The left panel shows the δ^{18}O offset (±5.7‰) necessary to significantly affect calculated meteoric water fractions, when using mCDW and meteoric water endmembers calculated from that data. The right panel shows the calculated meteoric water fractions produced using the original, and offset data. The calculated meteoric water fractions are impacted very little because two of the three endmembers (mCDW and meteoric water) are defined *by* the offset data.

A3 Uncertainty in calculated water fractions

Since meltwater fractions are calculated using analytical measures of salinity and $\delta^{18}O$, the accuracy and precision of these measurements are important. CTD salinity sensors have a reported precision of ±0.002. The Isotope Ratio Mass Spectrometer (IRMS; 1994 to 2014) measurements have a measured precision of ±0.04‰ based on replicates, while the Cavity Ring-Down Mass Spectrometer (CRDS) achieved a precision of ±0.02‰. The meteoric (GMW) endmember is arguably the least-well constrained, with glacial ice in West Antarctica ranging from -20‰ to -40‰, but much of that uncertainty has been eliminated by using the zero-salinity intercept determination on a $\delta^{18}O$-salinity mixing line, corroborated by nearby ice core values as discussed in the main manuscript. mCDW is well-constrained, based on many accurate in-situ measurements. Our sea ice melt endmember is adopted from previously published studies in the region (Meredith et al., 2008, 2010, 2013; Randall-Goodwin et al., 2015; Biddle et al., 2019).

We use Monte Carlo simulations to estimate uncertainty in water mass fraction calculations. We ran 10,000 simulations with input values varied randomly within these bounds and represent uncertainty by the standard deviation of the difference between the simulated, and initial runs. Observations were varied randomly by analytical precision above, also impacting the mCDW and meteoric water endmembers for each run. Additional perturbations are made to the endmember values; sea ice melt based on theoretical values (Rohling, 2013), meteoric water by the standard deviation of the ITASE01-2 ice core, mCDW salinity varied by the results of a spatial sensitivity analysis (**Appendix A4.2**) and $\delta^{18}O$ was varied by half the 95% prediction interval (~1σ) of the >200m $\delta^{18}O$-salinity relationship at the salinity maximum. Perturbations used in the uncertainty analysis are summarized in **Table A1.**

Table A1: Perturbations for uncertainty analysis. Perturbations are based on analytical precision for observations, the ITASE01-2 ice core for meteoric water, and theoretical values for sea ice melt (Rohling, 2013). mCDW perturbations are based on the 95% prediction interval of the >200m $\delta^{18}O$-salinity relationship at the salinity maximum, and salinity perturbations are based on the results of the spatial randomization analysis **(Appendix A4.2)**.

Parameter	Absolute Salinity perturbation (g/kg)	$\delta^{18}O$ perturbation (‰)
Observations	0.002	0.04 (0.02 for CRDS)
Meteoric water	N/A	1.9
Sea ice melt	2	0.1
mCDW, 1994	0.010*	0.010
mCDW, 2000	0.011	0.012
mCDW, 2007	0.009	0.018
mCDW, 2009	0.002	0.021
mCDW, 2014	0.015	0.013
mCDW, 2019	0.006	0.006
mCDW, 2020	0.017	0.004

* For 1994, we perturbed salinity by the average salinity standard deviation for the other years, to compensate for the smaller number of samples

The mean uncertainty in meteoric water fractions ranges from ±1.1 g/kg in 2019 to 1.7 g/kg in 2009, corresponding to average meteoric water column inventories uncertainty between ±0.5 m in 2019 and ±0.7 m in 2009 (**Table 3**). Meteoric water and sea ice melt fractions vary inversely, while mCDW fractions remain relatively stable. Calculations are most impacted by changes to the mCDW endpoint, as mCDW makes up ~99% of the (800m) water column on average; >95% in the meteoric water and sea ice melt rich surface waters, and >98% at all depths below 200 m.

14 samples from 2007 (3), 2009 (9), and 2014 (2) suggest negative meteoric water fractions, nine beyond the uncertainty described above. The negative meteoric water fractions result from high-salinity deep waters with $\delta^{18}O$ values less negative than the mCDW endpoint in the 3-endmember mixing model, reflective of uncertainty in the data and/or model limitations. Those years also display a wider spread in mCDW $\delta^{18}O$ than other years, likely due to evaporation during storage.

Sea ice melt and mCDW fractions are discussed in **Appendix A6**.

A4 Geographical sensitivity of endmembers and meteoric water column inventories

A4.1 Geographic clustering analysis

We analyzed the spatial sensitivity of results by splitting the study area into four groups and analyzing data from those groups for each year (**Figure A4, Table A2**). For each area, mCDW and meteoric water endmembers were defined based on only those data. In 10,000 Monte Carlo simulations, the observations and endpoints were perturbed by uncertainty associated with analytical precision and environmental variability (**Table A1**).

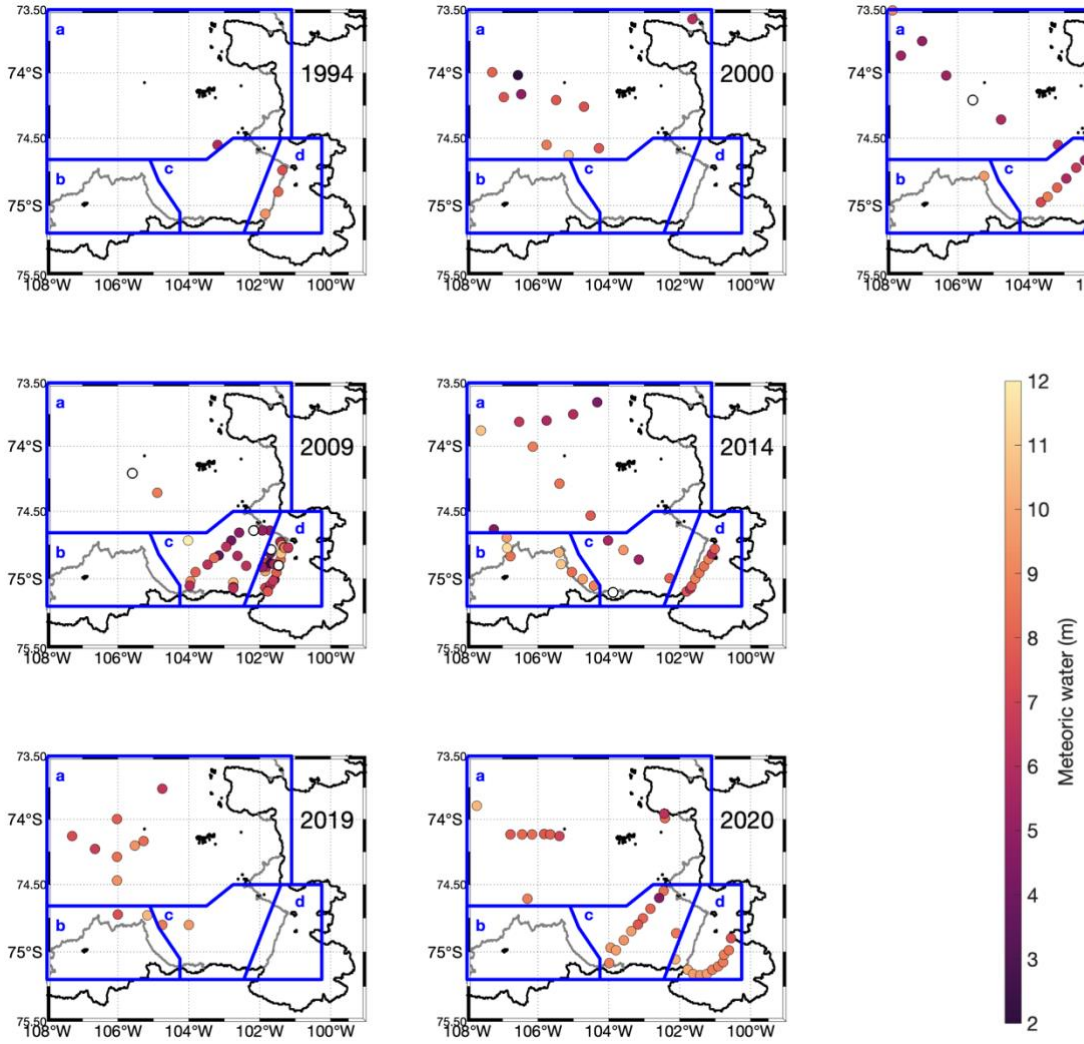

Figure A4: Sampling locations and geographic group boundaries for all years. Dot colors show meteoric water column inventory at individual stations, and outlines showing geographic groupings of stations for geographic sensitivity analysis (**Table A2**). Some locations provided only partial column inventories.

Table A2: Results of geographic grouping sensitivity analysis. mCDW is defined as the δ18O value at the salinity maximum falling on the linear regression of all salinity-$\delta^{18}O$ measurements deeper than 200m in each group of stations; meteoric water $\delta^{18}O$ is defined as the zero-salinity intercept on that same line. Uncertainty in mCDW δ18O is represented by half the 95% prediction interval at the salinity maximum (~1 σ), and uncertainty in salinity is the result of the randomization spatial sensitivity analysis, plus variation from perturbation of observations (**Appendix A4.2**). Average meteoric water inventory is the depth integration of the Gaussian fit of all calculated meteoric water fractions within each group, with uncertainty represented as the standard deviation in meteoric water fractions achieved using 10,000 Monte Carlo simulations perturbing the observations and endpoints by associated analytical and environmental uncertainty (**Table A1**). For each group of stations, mCDW and meteoric water endmembers used in meteoric water calculations are defined using only those data.

Year	Group	# of Stations	# of samples	mCDW absolute salinity (g/kg)	mCDW $\delta^{18}O$ (‰ vs VSMOW)	Meteoric water $\delta^{18}O$ (‰ vs VSMOW)	Average meteoric water column inventory (m)	Meteoric water fraction uncertainty (g/kg
1994	a	1	8	34.83±0.010	-0.02¬±0.02	-31.9±3.0	6.3±0.5	1.3
	d	3	18	34.86±0.010	-0.02¬±0.01	-28.3±2.0	8.0±0.6	1.6
2000	a	10	62	34.88±0.012	-0.05¬±0.01	-28.7±0.9	9.2±0.7	1.7
2007	a	8	34	34.90±0.009	-0.04¬±0.02	-26.1±1.4	8.4±0.8	1.8
	b	1	4	34.85±0.009	-0.05¬±0.63	-29.7±2.7	10.3±0.8	1.5
	c	6	36	34.87±0.010	0.01¬±0.04	-32.1±1.4	9.0±0.7	1.6
2009	a	2	4	34.87±0.003	0.01¬±0.7	-43.7±4.8	7.0±0.6	1.1
	c	18	61	34.87±0.003	-0.01¬±0.04	-28.8±1.1	8.7±0.8	1.8
	d	26	110	34.87±0.002	0.02¬±0.03	-29.0±0.7	8.5±0.7	1.7
2014	a	9	57	34.86±0.015	0.04¬±0.03	-27.2±1.2	8.3±0.6	1.8
	b	8	61	34.87±0.015	0.07¬±0.02	-32.1±1.0	10.1±0.7	1.5
	c	5	19	34.83±0.015	0.06¬±0.02	-33.6±2.0	7.9±0.5	1.4
	d	9	76	34.83±0.015	0.06¬±0.02	-31.7±1.1	7.5±0.5	1.4
2019	a	8	68	34.89±0.006	-0.1¬±0.01	-27.6±0.6	8.2±0.6	1.2
	b	2	21	34.87±0.006	-0.12¬±0.01	-30.6±0.8	10.0±0.7	1.1
	c	2	18	34.85±0.006	-0.11¬±0.02	-31.5±1.0	8.2±0.5	0.9
2020	a	10	90	34.89±0.016	-0.11¬±0.01	-28.2±0.4	8.7±0.6	1.3
	c	11	70	34.86±0.017	-0.12¬±0.01	-29.6±0.5	8.7±0.5	1.2
	d	11	120	34.85±0.017	-0.13¬±0	-29.7±0.4	8.5±0.5	1.1

mCDW (as defined in Appendix A1) was broadly shows little geographic sensitivity. In all years, salinity varied by less than observed seasonal salinity variation in mCDW (0.01 g/kg; Mallett et al., 2018). mCDW $\delta^{18}O$ exhibited less variation than that associated with instrumental precision.

The meteoric water $\delta^{18}O$ fingerprint calculated for different geographic groupings each year is not geographically sensitive – as would be expected with deep meteoric water (basal meltwater) having a single source. 2009 Group a rendered a significantly different meteoric water endmember, however this number is based on data from just 4 samples (3 from >200 m); given the data limitations and the sample quality issues for 2009, it is unlikely that the -43.7±4.8‰ endmember is representative.

In general, the meteoric water column inventories appear insensitive to geographic groupings. The exceptions are Group a in 1994 and 2009, and Group b in 2007, 2014, 2019. In 1994, Group a contains

only a single station in 1994 (8 samples), and only 4 samples (2 stations) in 2009. Group b consists of those samples collected alongside TIS; locations likely to be dominated by meltwater originating from beneath PIIS (Wåhlin et al., 2021). Surprisingly, given the small number of samples collected near TIS in 2007 and 2019, the meteoric water inventories from Group b stations are consistent.

A4.2 Spatial randomization analysis

A geographic sensitivity Monte Carlo analysis involved calculating results from random sets of 3 stations 10,000 times (**Table A3**). For each group of 3 stations, mCDW and meteoric water endmembers, and average meteoric water column inventories were calculated using only those data. Stations with fewer than 2 samples >200 m were excluded. As the 3-endmember mixing model is most sensitive to the mCDW endmember, a set of stations lacking samples >800m (deeper than the sub-cavity ridge; 'pure' mCDW) had a random mCDW sample from >800m that year added to the data set for analysis.

Table A3: Results of station randomization sensitivity analysis. mCDW is defined as the $\delta^{18}O$ value at the salinity maximum on the linear regression of all salinity-$\delta^{18}O$ measurements deeper than 200 m in each group of stations; meteoric water $\delta^{18}O$ is defined as the zero-salinity intercept on that same line. Average meteoric water inventory is the depth integration of the Gaussian fit of all calculated meteoric water fractions within each group. In all cases, uncertainty is represented by the standard deviation in the results obtained across 10,000 Monte Carlo simulations for each year. 1994 had only 4 stations, variability represented by this analysis for that year may be artificially low.

YEAR	Mean mCDW salinity (g/kg)	Mean mCDW $\delta^{18}O$ (‰)	Mean meteoric water $\delta^{18}O$ (‰)	Mean meteoric water inventory (m)	% Meteoric water inventory uncertainty	Meteoric water fraction uncertainty (g/kg)
1994*	34.86±0	-0.01±0.01	-29.4±0.6	7.6±0.2	2.9%	0.1
2000	34.87±0.03	-0.06±0.03	-28.7±1.6	8.8±0.5	5.4%	0.8
2007	34.89±0.01	-0.03±0.04	-27.9±3.4	9.0±0.7	7.3%	1.1
2009	34.86±0.06	-0.01±0.08	-28.7±4.1	8.8±0.7	8.0%	1.8
2014	34.84±0.03	0.05±0.05	-31.1±3.3	8.5±0.8	9.4%	1.1
2019	34.88±0.01	-0.10±0.01	-29.6±1.6	8.5±0.4	4.9%	0.6
2020	34.87±0.02	-0.11±0.02	-29.1±1.4	8.8±0.6	6.3%	0.7

The mCDW properties appear geographically insensitive, though 2009 and 2014 exhibit higher variability than other years, potentially due to sample collection and/or storage issues (**Appendix A2, A7**).

Meteoric water endmember properties showed greater spatial variability in 2007, 2009, 2014. In these 3 years, the data show the greatest scatter, and station locations do not always have mCDW samples near the seafloor. The lengthy meteoric water endmember extrapolation benefits from many samples collected below 200 m.

The impact of sample geographic location variability is generally comparable to that of the primary uncertainty analysis (analytical precision and environmental variability), with the exceptions of 2009 and 2014. However, the 2014, spatial uncertainty is somewhat inflated due to the very high (>10m) meteoric water inventories at stations immediately alongside TIS, while the 2009 data are impacted by sample storage issues, and poor depth resolution at some locations.

A5 The impact of precipitation on meteoric water inventories

Sea-level precipitation at this latitude has $\delta^{18}O$ values of ~-15‰ (based on snow collected during NBP19-01, consistent with expected local values from other studies; Gat and Gonfiantini, 1981; Ingraham, 1998; Noone and Simmonds, 2002; Masson-Delmotte et al., 2008). This region of the Amundsen Sea receives ~0.5 m water equivalent of precipitation per year (Donat-Magnin et al., 2021), and mCDW on the shelf has a residence time of ~2 years (Tamsitt et al., 2021). We recalculated water column meteoric water inventories assuming 1 m (2 full years) of local precipitation (-15‰ $\delta^{18}O$) in the upper 200 m of the water column at the time of sampling.

We find that adding 1 m of precipitation to the water column decreases the amount of meteoric water (as defined using the zero-salinity intercepts, **Figure 2**) by an average of 0.55±0.01 m, and decreases sea ice melt by an average of 0.57 ±0.03 m (**Table A4**). These results suggest that even with two years' worth of precipitation present in the water column at the time of sampling, the calculated meteoric water inventory could consist of >92% glacial meltwater.

Table A4: Impact of precipitation on total meteoric water column inventory. Mean meteoric water inventory is the integrated mean meteoric water content between the surface and 800m. The upper water column will include meteoric water from both precipitation, and GMW introduced at depth and mixed upward. The three rightmost columns in the table show the impact on meteoric and sea ice melt water column inventories of recalculating column inventories (meteoric water ~-30‰ $\delta^{18}O$, **Table 2**) assuming 2 years of precipitation (~-15‰ $\delta^{18}O$) in the water column at the time of sampling.

		Impact of 1 m (~2 years) precipitation (-15‰ $\delta^{18}O$)		
Year	**Mean meteoric water inventory (m)**	**Change in (glacial) meteoric water (m)**	**Change in sea ice melt water (m)**	**Estimated water column glacial meteoric water**
1994	7.62	-0.56	-0.61	92.6%
2000	9.16	-0.57	-0.62	93.8%
2007	8.95	-0.56	-0.55	93.7%
2009	8.57	-0.55	-0.55	93.5%
2014	8.93	-0.54	-0.55	94.0%
2019	8.42	-0.54	-0.57	93.6%
2020	9.18	-0.56	-0.54	93.9%

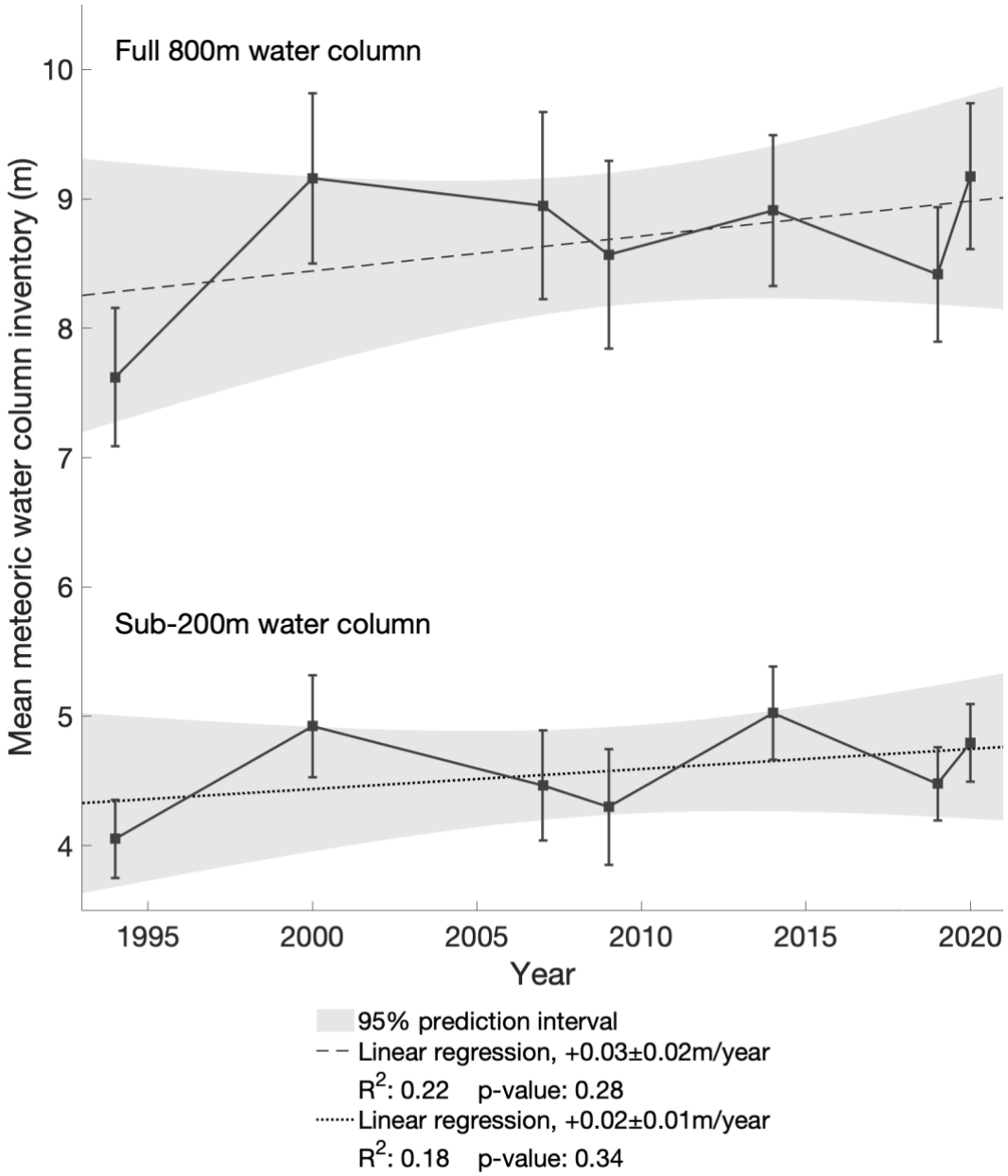

Figure A5: Mean meteoric column inventory for each sampled year. Points represent the depth-integrated meltwater volume from the Gaussian Process fit (grey lines in **Figure 3**) between 200 and 800 m depth. Error bars show the uncertainty in mean meteoric water column inventory associated with analytical precision and environmental variability (**Data and Methods 2.2**). The relative year-to-year inventories here show the same general empirical trend (within uncertainty) as **Figure 4**. 2014 shows the highest sub-200m meteoric water content, owed to the sampling immediately alongside TIS - directly in the pathway of glacial meltwater from PIIS (Wåhlin et al., 2021).

Figure A5 and **Table A5** show a comparison of the yearly inventories in the total water column vs the water column deeper than 200 m. Both the full and partial water columns show the same relative trend in meteoric water content, indicating that the observed variability is not an effect of interannual variability in precipitation.

Table A5: Relative Fractions of yearly meteoric water inventory in the 800m and 200-800m water columns. Reported column inventories are the depth integration of the Gaussian fit of all measurements in the field area between the specified depths. The Relative fraction is the normalized relative volume of the average inventory from year to year.

	0 m – 800 m		200 m – 800 m		Fraction of total meteoric water in upper 200 m
Year	**Column Inventory, meteoric water (m)**	**Normalized relative fraction**	**Column Inventory, meteoric water (m)**	**Normalized relative fraction**	
1994	7.6±0.5	83±6	4.1±0.3	81±6	45.9%
2000	9.2±0.7	100±7	5.0±0.4	98±8	45.4%
2007	9.0±0.7	97±8	4.5±0.5	89±9	49.2%
2009	8.6±0.7	93±8	4.4±0.5	86±9	48.9%
2014	8.9±0.6	97±6	5.1±0.4	100±7	42.7%
2019	8.4±0.5	92±6	4.6±0.3	89±6	45.9%
2020	9.2±0.6	100±6	4.9±0.3	95±6	46.9%

A6 Sea ice melt and mCDW fractions

A6.1 Sea ice melt

While the primary focus of discussion in this paper is meteoric water, the three-endmember mixing model also yields sea ice meltwater fractions. In locations where integrated sea ice melt fractions are negative, net sea ice formation at the time of sampling is indicated. Using a less negative meteoric water $\delta^{18}O$ endmember (e.g. -25‰ used in Biddle et al., 2019) will result in higher meteoric water fractions and lower sea ice melt fractions, significantly impacting areas/years of net sea ice melt/formation (**Figure A7**). Since >92% of the meteoric water content in the study area is estimated to be basal melt, using a GMW meteoric water endmember (or close to) will produce more accurate net sea ice melt/formation inventories (and correspondingly more accurate meteoric water inventories).

In 2007, 2009, and 2014 positive ice melt fractions >200 m, likely the resulted from samples compromised before analysis. Evaporation leads to positive fractionation of seawater $\delta^{18}O$, leading to a less-depleted $\delta^{18}O$ observation at time of analysis; less depleted $\delta^{18}O$ relative to salinities fresher than mCDW will be interpreted by the 3-endmember mixing model as sea ice melt. The stratification in this region makes it unlikely that there are significant sea ice melt fractions below 200 m. As with the $\delta^{18}O$-salinity (**Figure 2**) and meteoric water-depth (**Figure 3**) plots, 1994, 2000, 2019 and 2020 exhibit the tightest distribution, suggesting higher quality data. Grey lines show the Gaussian process fit, and points are shaded to show sample $\delta^{18}O$.

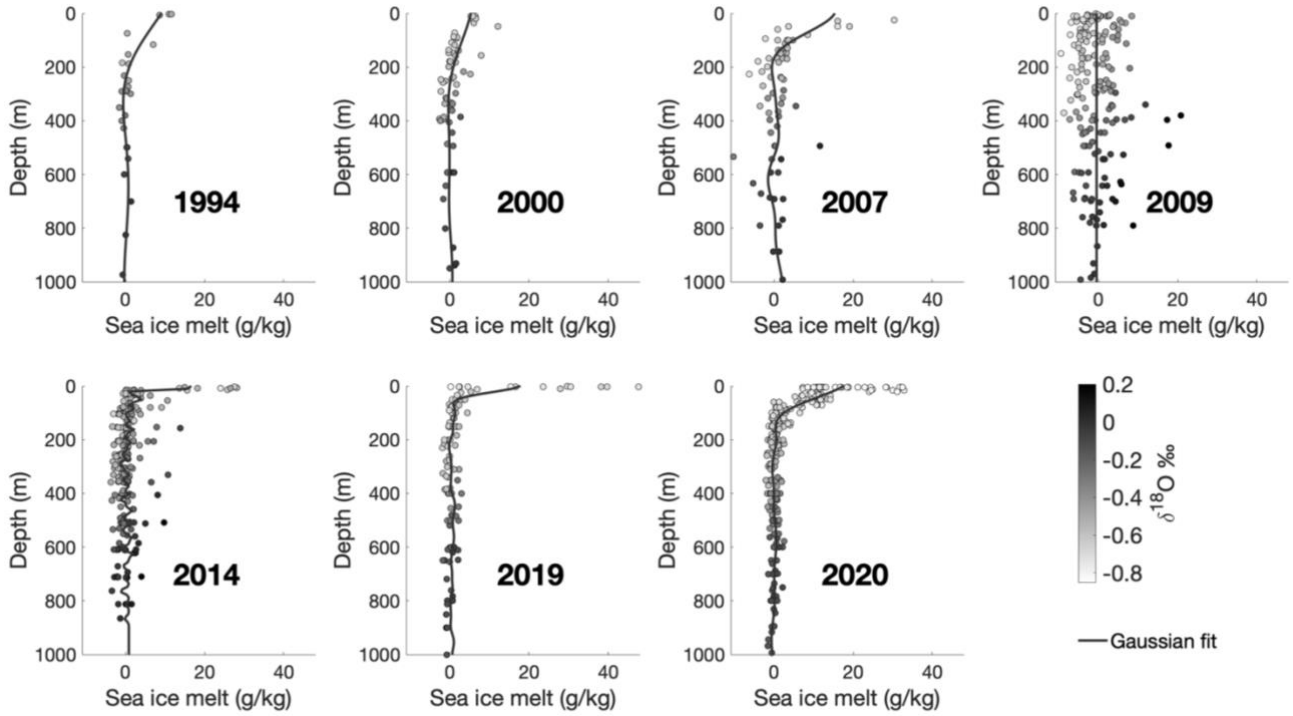

Figure A6: Sea ice melt fractions vs depth. Calculated sea ice melt fractions using salinity and $\delta^{18}O$ measurements in 3-endmember mixing model. Shading of dots indicates the measured $\delta^{18}O$ of that sample. In several years (2014-2020) there is a high concentration of sea ice melt near the surface, and very little extending deeper than 200 m. Negative values indicate net sea ice formation. Years with greater sea ice melt (2007, 2020) than sea ice formation show greater divergence from the mCDW-GMW mixing line in surface waters (**Figure 2**).

Table A6: Sea ice melt column inventories and uncertainty. Mean sea ice melt column inventories are produced by depth integrating the Gaussian process fit (grey lines **Figure A6**) between the surface and 800m. Uncertainty as described in **Appendix A3.**

Year	Mean sea ice melt column inventory (m)	Sea ice melt fraction uncertainty (g/kg)
1994	1.0¬±0.8	1.9
2000	0.6¬±0.9	2.1
2007	1.2¬±0.9	2.2
2009	-0.4¬±1.0	2.2
2014	0.5¬±0.9	2.0
2019	1.0¬±0.7	1.4
2020	1.1¬±0.8	1.7

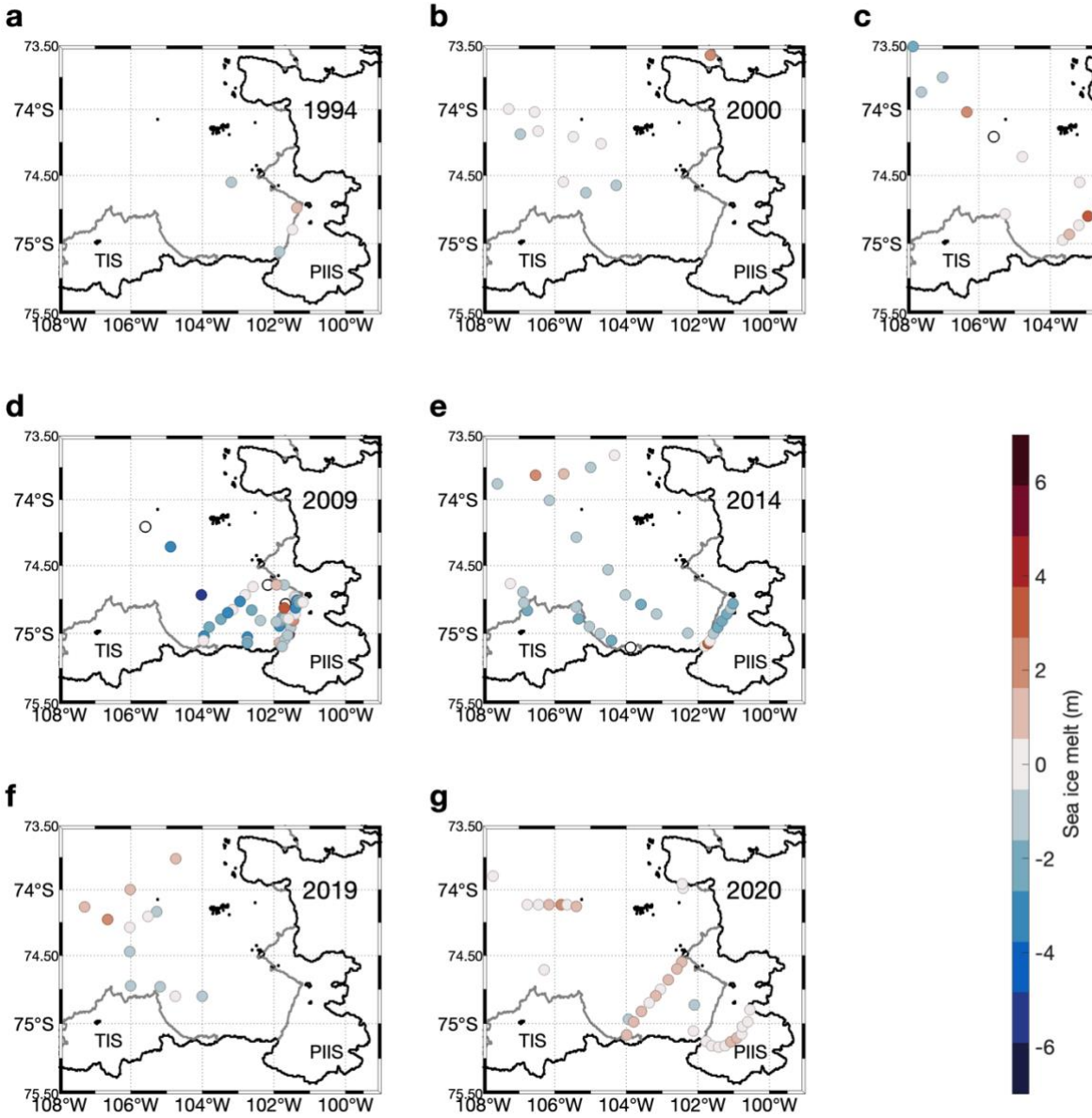

Figure A7: Integrated sea ice melt fractions at sampling locations each year. Negative sea ice melt fractions indicate areas of net sea ice formation. Stations with partial water column sampling show only partial inventories. White dots with black outlines are stations where only one depth was sampled (2007, 2009, 2014). Years with greater sea ice melt (2007, 2020) than formation show greater divergence from the mCDW-GMW mixing line in surface waters (**Figure 2**).

A6.2 mCDW fractions

Waters deeper than ~800m are comprised of pure mCDW; moving toward the surface, meteoric freshwater from basal melt is introduced starting at ~700m. The near surface waters are rich in meteoric water and/or sea ice melt are comprised of >92% mCDW (**Figure A8**).

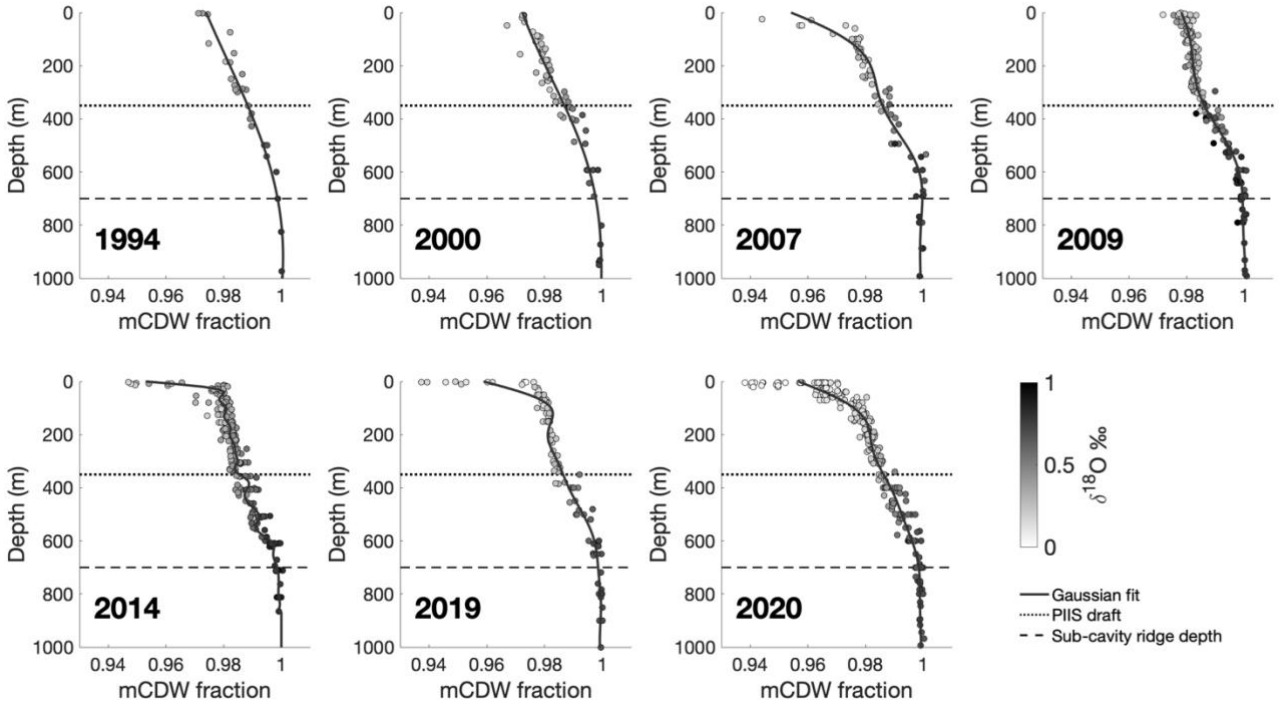

Figure A8: mCDW fractions vs depth. Calculated mCDW fractions using salinity and $\delta^{18}O$ measurements in 3-endmember mixing model. Shading of dots indicates the measured $\delta^{18}O$ of that sample. Deep waters (>800m) characterize relatively unadulterated mCDW, while near surface waters contain the highest concentrations of sea ice melt and meteoric water. Dotted horizontal lines show the depth of the PIIS draft, and dashed lines show the depth of the PIIS sub-cavity ridge.

Table A7: mCDW column inventories and uncertainty. Mean sea ice melt column inventories are produced by depth integrating the Gaussian process fit (grey lines **Figure A8**) between the surface and 800m. Uncertainty as described in **Appendix A3.**

Year	Mean mCDW column inventory (m)	mCDW fraction uncertainty (g/kg)
1994	781.2±0.3	0.6
2000	780.1±0.4	0.6
2007	779.8±0.3	0.7
2009	781.6±0.2	0.6
2014	780.4±0.5	0.7
2019	780.6±0.2	0.5
2020	779.6±0.5	0.8

A7 2009 Sample quality control

A subset of the samples for 2009 were analyzed on an IRMS in 2010, while the remainder were stored until a 2020 CRDS analysis. At the latter time, 56% of the samples analyzed contained an unknown, clear, needle-shaped precipitate. Several bottles also had a lower-than-expected sample volume, suggesting evaporation, which would likely have altered the $\delta^{18}O$ content via isotopic fractionation. Several steps were taken to ensure the quality of samples analyzed after a decade in storage.

A7.1 SEM EDS Analysis of Precipitate

Samples of the precipitate were extracted from multiple sample bottles and analyzed using a Scanning Electron Microscope, equipped with a FEI Magellan 400 XHR SEM with Bruker Quantax XFlash 6 | 60 SDD EDS detector, at the Stanford Nano Shared Facilities (SNSF). Peaks were observed at the spectra associated with Mg, Si, and O, indicating the precipitate is likely some form of Magnesium Silicate Hydroxide ($Mg_3Si_2O_5(OH)_4$), or Magnesium Silicate Hydrate ($Mg_2Si_3O_8{\bullet}H_2O$). $Si(OH)_4$ is the simplest soluble form of silica and is found universally in seawater at low concentrations (Belton et al., 2012). The maximum amount of silicate that could be expected in this area of the ocean is ~100 µmol/kg (Rubin et al., 1998). In this case, even if the entire 100 µmol/kg of Si were drawn down to 0, solely into a Magnesium Silicate, with a very high fractionation factor, e.g. the -40‰ reported for diatoms (Leclerc and Labeyrie, 1987) the greatest effect on a sample would be 0.0003‰ – well below the analytical precision of the CRDS (0.025‰) or IRMS (0.04‰). Therefore, it is highly unlikely that the precipitate contributed a detectable fractionation or alteration of seawater $\delta^{18}O$ in our samples.

A7.2 Quality control for evaporation

In all years, the bulk of the $\delta^{18}O$ data fall in a broadly predictable pattern, less depleted at depths below ~600m, and more depleted near the surface. Values >2 standard deviations from this pattern denote samples that were likely subject to significant evaporation (**Figure A9**)

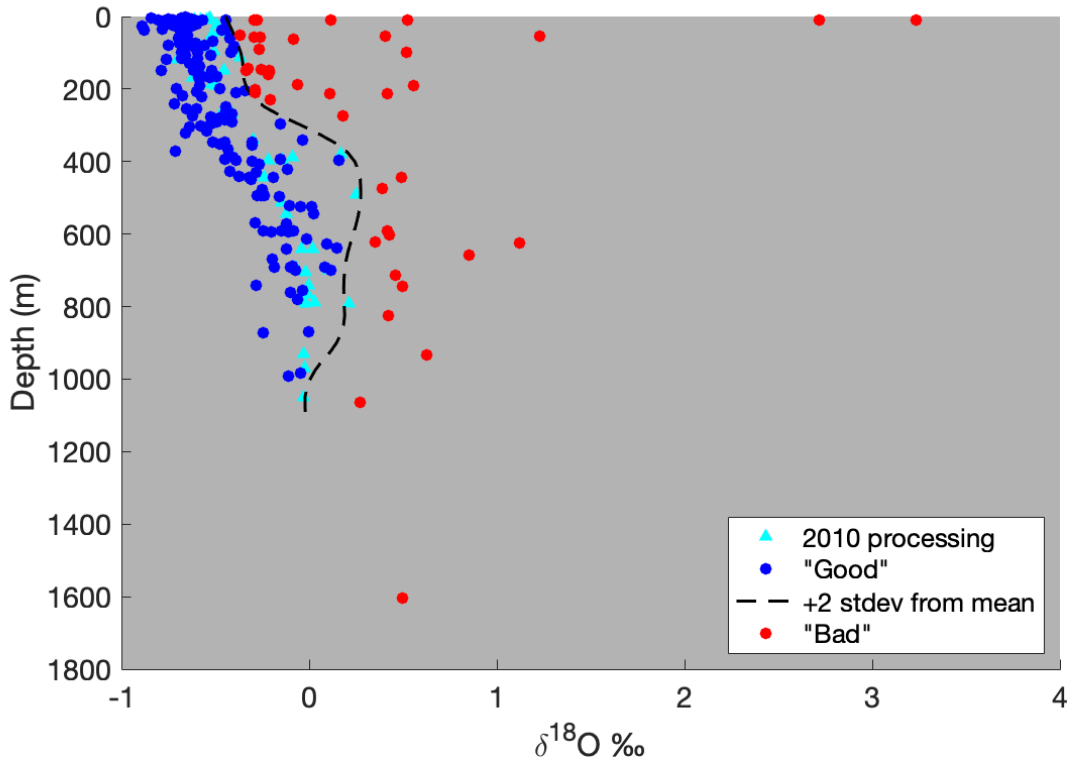

Figure A9: δ^{18}O vs depth for all 2009 samples, coded for likelihood of evaporation. The dashed line represents +2 standard deviations from a moving depth-averaged δ^{18}O based on the 2010 processing, beyond which the results are unacceptable. Archivable data will be made available upon publication.

As a secondary check, the δ^{18}O of all samples was plotted vs depth with a qualitative indicator of the amount of precipitate found in the sample vial (**Figure A10**) to see if any patterns emerged compared to that of depth-comparable samples processed in 2010. No clear trend was evident.

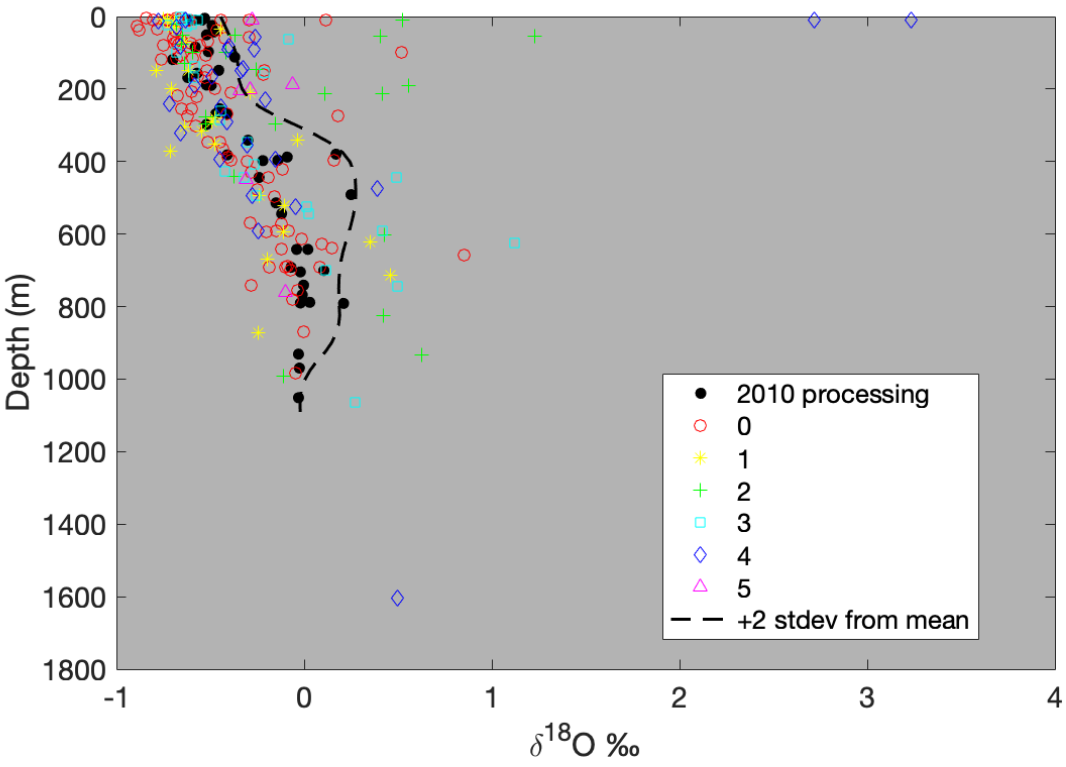

Figure A10: $\delta^{18}O$ vs depth of all 2009 samples, coded by amount of precipitate present. Each bottle was graded by eye based on the volume of precipitate present with 0 being no precipitate present, and 5 being the most precipitate present. As with **Figure A9**, the dashed line represents +2 standard deviations from the mean $\delta^{18}O$ at each depth.

Evaporation is accompanied by isotopic fractionation, with $H_2{}^{16}O$ evaporating preferentially, leaving the remaining liquid relatively enriched in the $H_2{}^{18}O$. Evaporation also increases the salinity and thus density of the remaining sample. We measured the density of each seawater sample 5 times using a calibrated 1ml pipet and mg balance. The theoretical density of each sample was calculated from its associated CTD salinity and temperature. Differences between measured and theoretical densities for each sample are plotted in **Figure A11**.

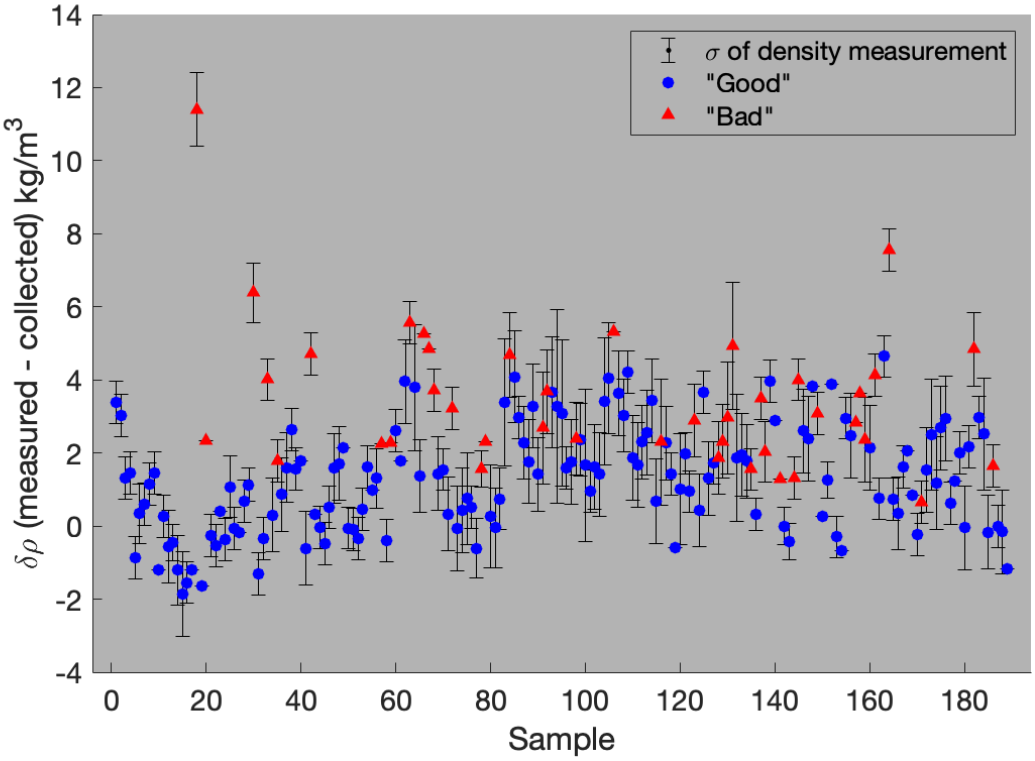

Figure A11: Difference in measured density vs theoretical density for each 2009 sample analyzed in 2020. Theoretical density is based on CTD salinity at each sample location, and measured density calculated from 1ml sample aliquots weighed on a mg scale, with sample coding as in **Figure A9**. Error bars represent the standard deviation of replicates for each measurement.

While a few samples show clear evidence of evaporation, and correspondingly high $\delta^{18}O$ values, most show less obvious density anomalies, exposing the limitations of our scale accuracy at that level. 75% of the samples measured showed a higher than expected density and 25% measured a lower than expected. **Figure A11** displays a significant overlap in measured density space between samples previously identified as "good" or "bad" (**Figure A9**). **Figure A11** shows that there are no samples flagged as compromised ("bad") from our earlier depth-based analysis with a $\delta\rho$ greater than 1.3 kg/m^3. At an aggressive first pass, we removed all sample data with a $\delta\rho$ greater than 1.3 kg/m^3 and looked at each hydrocast profile individually, using the remaining data. Excluded samples flagged as "good" were returned to the dataset, and individual profiles re-scrutinized individual profiles to check for any qualitative anomalies.

A7.3 Conclusion and final 2009 sample inclusion

While it is very unlikely that the precipitate changed sample values, some samples do appear to have been subject to evaporation. The inclusion of all samples flagged as "Good" does not qualitatively

change our analyses when compared with the data processed in 2010. We exclude the 41 samples initially flagged as "Bad," (**Figure A9**) and retain the remaining 148 flagged as "Good".

A8 CRDS and IRMS cross-calibration

We processed 100 samples from 2019 and 2020 concurrently using the Picarro L2140-i CRDS, and on a Finnigan MAT252 IRMS (**Figure A12**) using CO_2 equilibration (Epstein and Mayeda, 1953). Both instruments were independently calibrated using international standards VSMOW, SLAP, and GISP, and all samples were run in duplicate. The data from both machines was comparable, with the Picarro achieving a precision of 0.02‰, and the IRMS achieving a precision of 0.03‰ on replicates. The offset between CRDS and IRMS data averaged -0.02‰, with the CRDS data being more negative. Since the offset between the two machines was less than either instrument's precision, data from the CRDS was used as-is. Values reported for the CRDS are the average of 6 individual injections/measurements from each vial; reported precision is based on the standard deviation between multiple 6-injection averages from replicate analyses, separated by days, weeks, or months.

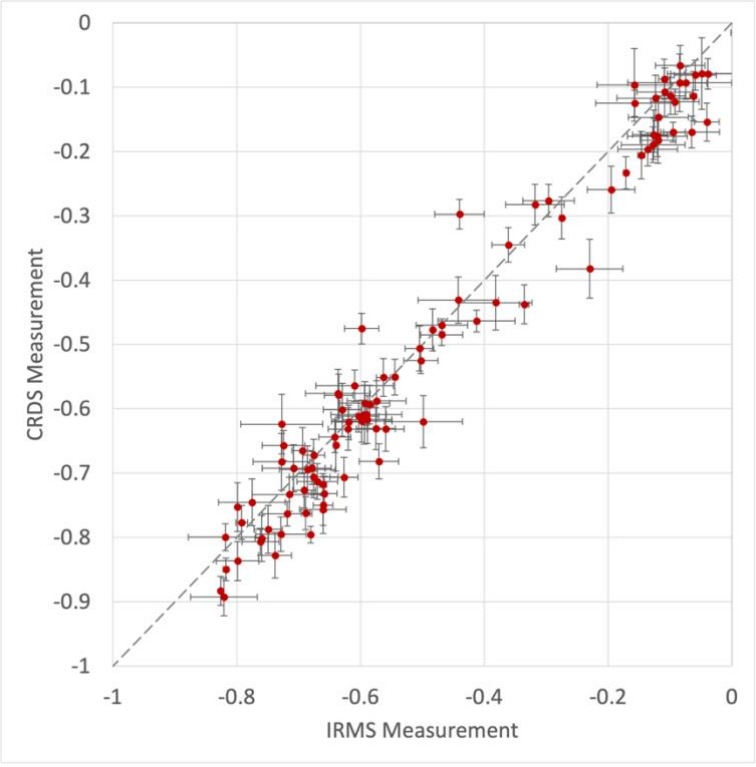

Figure A12: 101 seawater $\delta^{18}O$ samples collected in 2019 and 2020 analyzed with both CRDS and IRMS. Each point represents the value obtained by measuring the same sample on the IRMS (x-axis) and the CRDS (y-axis). Error bars represent the corresponding standard deviation of the IRMS and CRDS measurements. The dashed grey line is a 1:1 slope.

A9 CRDS Methods

570 of the isotope samples for this study (all samples from 2019 and 2020, portions from 2007 and 2009) were run on a Picarro L2140-i CRDS system, rather than a traditional IRMS. Using this system, we were able to achieve an average precision of <0.02‰ on multiple replicate analyses.

Samples were collected in 10ml or 30ml glass serum vials (Fisher Scientific part number: 06-406D/06-406F), sealed with rubber stoppers (Fisher Scientific part number: 06-406-11B) and aluminum seals (Fisher Scientific part number: 06-406-15).

Sample vials should be filled to just below the "neck" (narrowest part). Minimizing the headspace of the vial is important for minimizing evaporation, however it is important to leave *some* headspace to allow for expansion/contraction of the sample (if collecting samples larger than 30 ml, slightly more headspace should be left, with 250 ml vials being filled to ~1/2 way up the "shoulder" before the neck). When sealing serum vials with rubber stoppers and aluminum seals, it is important that the tops of the aluminum seals are crimped tightly but remain flat after crimping/capping. An upward "buckling" of the aluminum seal indicates over-crimping and will produce an inferior seal.

Internal lab (Stanford SIL) data shows that samples can be preserved in this manner for up to 5 years without significant degradation, while bottles with threaded caps and parafilm reliably maintain sample integrity below instrumental precision for no more than 1 year.

The instrument setup used was as follows:

- 10µl syringe (Trajan Part number: 002982)
- A single standard or unknown run consists of 7 injections (measurements) per sample
- Sample injection volume 2.2 µl
- 3x 5µl rinses with fresh water from inkwell (IW) between each sample
- 3x 2.2µl rinses with sample before first measurement of new sample or standard vial
- Rinse only between sample vials, or 1 rinse for every 7 standard or unknown injections.

Several protocols were also followed with regards to sample and instrument handling.

- Fresh vial of internal lab standard (ILS) used each day. The ILS was prepared to have a $\delta^{18}O$ in the middle of the range expected from the unknowns (i.e. ~-0.3‰) to minimize memory issues between samples. The IW was also filled with water of approximately this composition.
- A fresh 2ml vial of ILS was used each day and discarded at the end of the sequence.
- Samples were pipetted from sealed 10ml or 30ml serum into 2ml vials (Fisher Scientific part number: 03-391-15) for analysis on the day they were to be analyzed. The 2ml vials used for analysis were found to only reliably preserve sample $\delta^{18}O$ for <1 week.

- After each sequence, the syringe was cleaned with DI water, and then rinsed thoroughly with water from the Inkwell, to minimize memory/contamination issues of residual water left in the syringe.
    - Treated in this way, syringes can be expected to last for 1500 to 2500 injections
- Fresh vaporizer septa (Trajan Part number: 0418240) was used every day
- ILS were analyzed no less than every 5th unknown, and no fewer than 3 ILS were measured per run
    - An ILS
- All data were corrected based on the slope of the ILS measurements over the course of the sequence.
- Each run began with no fewer than 10 injections from the IW, to allow the instrument to reach baseline.
- Syringe cleaned thoroughly with DI water each day, and manually rinsed with IW water prior to sequence.
- No more than 5 unknowns (7 injections each) measured between run of ILS (7 injections)
- ILS measured at least 3 times during each sequence – at the beginning, end, and midpoint. least 3 standards measured during each sequence.

A typical 24h sequence ran 16 unknowns. The sequence was set up, as follows:

- 15 injections from IW
- ILS (7 injections)
- 4 unknowns (4x7 injections)
- ILS (7 injections)
- 4 unknowns (4x7 injections)
- ILS (7 injections)
- 4 unknowns (4x7 injections)
- ILS (7 injections)
- 4 unknowns (4x7 injections)
- ILS (7 injections)

Overall, this sequence consists of 162 injections, 112 of which contained salt, for a vaporizer load of ~8.6 mg of salt/day. The instrument vaporizer was cleaned at least every 200mg worth of salt injected.

- @ 35PSU & 2.2µl injections, this is 2597 salty injections, or 371 samples @ 7 injections each. (~ every 23 analytical days)

Finally, analytical data quality control was conducted in the following way

- The first injection of each sample was discarded, to minimize instrument memory issues
- If the standard deviation of the remaining 6 injections was >0.04‰, up to one outlier could be removed. Any samples where the standard deviation of measured values was still >0.04‰ were rerun the following day from the same vial, using the same septa.
- If a rerun would not be possible the following day, the vial septa was replaced with a new one.
- Data from each hydrocast were inspected as a group. Any samples that appeared inconsistent with the rest of the hydrocast (e.g. with regards to salinity, or neighboring $\delta^{18}O$ values) were rerun. If the rerun occurred within 1 week of the initial run, the same vial was used. Otherwise, a fresh aliquot of sample was drawn from the resealed serum vial.

Data availability

All data, excluding that flagged as "bad," (**Appendix A7**) used in this study can be accessed at: https://doi.org/10.25740/zf704jg7109

Author contributions:

Conceptualization: RBD
Methodology: RBD, ANH, DAM
Investigation: ANH, DAM, RBD
Visualization: ANH
Funding acquisition: RBD
Project administration: RBD
Supervision: RBD
Writing – original draft: ANH
Writing – review & editing: ANH, SSJ, RBD, DAM, RAM
Contribution of data: ANH, DAM, RBD, SSJ, RAM

Competing interests

The authors declare that they have no conflict of interest.

Acknowledgments

We acknowledge the staff and crew of Nathaniel B. Palmer cruises 94-02, 00-01, 07-02, 09-01, 19-01, 20-02, and iSTAR2014 for assistance with data acquisition. We extend special thanks to Isa Rosso, Michael Burnett, and Emilia Fercovic for their help with sample collection. MAC3 Impact Philanthropies assisted with CRDS instrumentation and development. Peter Schlosser & Ronny Friedrich provided the 2007 CRDS data, and Shigeru Aoki was consulted regarding the 2014 data offset. Thanks also to Cindy Ross and Stanford Nano Shared Facilities, supported by NSF ECCS-2026822 for SEM analyses.

Funding: This project was funded by NSF:
NSF-OPP-1644118
NSF-OPP-1644159

References

Adusumilli, S., Fricker, H. A., Medley, B., Padman, L., and Siegfried, M. R.: Interannual variations in meltwater input to the Southern Ocean from Antarctic ice shelves, Nat. Geosci., 13, 616–620, https://doi.org/10.1038/s41561-020-0616-z, 2020.

Araguás-Araguás, L., Froehlich, K., and Rozanski, K.: Deuterium and oxygen-18 isotope composition of precipitation and atmospheric moisture, Hydrol. Process., 14, 1341–1355, https://doi.org/10.1002/1099-1085(20000615)14:8<1341::AID-HYP983>3.0.CO;2-Z, 2000.

Assmann, K. M., Hellmer, H. H., and Jacobs, S. S.: Amundsen Sea ice production and transport, J. Geophys. Res. Oceans, 110, https://doi.org/10.1029/2004JC002797, 2005.

Belton, D. J., Deschaume, O., and Perry, C. C.: An overview of the fundamentals of the chemistry of silica with relevance to biosilicification and technological advances, Febs J., 279, 1710–1720, https://doi.org/10.1111/j.1742-4658.2012.08531.x, 2012.

Benetti, M., Sveinbjörnsdóttir, A. E., Ólafsdóttir, R., Leng, M. J., Arrowsmith, C., Debondt, K., Fripiat, F., and Aloisi, G.: Inter-comparison of salt effect correction for δ18O and δ2H measurements in seawater by CRDS and IRMS using the gas-H2O equilibration method, Mar. Chem., 194, 114–123, https://doi.org/10.1016/j.marchem.2017.05.010, 2017.

Biddle, L. C., Heywood, K. J., Kaiser, J., and Jenkins, A.: Glacial Meltwater Identification in the Amundsen Sea, J. Phys. Oceanogr., 47, 933–954, https://doi.org/10.1175/JPO-D-16-0221.1, 2017.

Biddle, L. C., Loose, B., and Heywood, K. J.: Upper Ocean Distribution of Glacial Meltwater in the Amundsen Sea, Antarctica, J. Geophys. Res. Oceans, 124, https://doi.org/10.1029/2019JC015133, 2019.

Blunier, T. and Brook, E. J.: Timing of Millennial-Scale Climate Change in Antarctica and Greenland During the Last Glacial Period, Science, 291, 109–112, https://doi.org/10.1126/science.291.5501.109, 2001.

Boisvert, L. N., Webster, M. A., Petty, A. A., Markus, T., Cullather, R. I., and Bromwich, D. H.: Intercomparison of Precipitation Estimates over the Southern Ocean from Atmospheric Reanalyses, J. Clim., 33, 10627–10651, https://doi.org/10.1175/JCLI-D-20-0044.1, 2020.

Brown, P. J., Meredith, M. P., Jullion, L., Naveira Garabato, A., Torres-Valdés, S., Holland, P., Leng, M. J., and Venables, H.: Freshwater fluxes in the Weddell Gyre: results from δ18O., Philos. Transact. A Math. Phys. Eng. Sci., 372, 20130298, https://doi.org/10.1098/rsta.2013.0298, 2014.

Coplen, T. B.: Reporting of stable hydrogen, carbon, and oxygen isotopic abundances (Technical Report), Pure Appl. Chem., 66, 273–276, https://doi.org/10.1351/pac199466020273, 1994.

Dansgaard, W.: Stable isotopes in precipitation, Tellus, 16, 436–468, https://doi.org/10.3402/tellusa.v16i4.8993, 1964.

Dierssen, H. M., Smith, R. C., and Vernet, M.: Glacial meltwater dynamics in coastal waters west of the Antarctic peninsula, Proc. Natl. Acad. Sci., 99, 1790–1795, https://doi.org/10.1073/pnas.032206999, 2002.

Donat-Magnin, M., Jourdain, N. C., Kittel, C., Agosta, C., Amory, C., Gallée, H., Krinner, G., and Chekki, M.: Future surface mass balance and surface melt in the Amundsen sector of the West Antarctic Ice Sheet, The Cryosphere, 15, 571–593, https://doi.org/10.5194/tc-15-571-2021, 2021.

Dotto, T. S., Naveira Garabato, A. C., Bacon, S., Holland, P. R., Kimura, S., Firing, Y. L., Tsamados, M., Wåhlin, A. K., and Jenkins, A.: Wind-Driven Processes Controlling Oceanic Heat Delivery to the Amundsen Sea, Antarctica, J. Phys. Oceanogr., 49, 2829–2849, https://doi.org/10.1175/JPO-D-19-0064.1, 2019.

Dutrieux, P., De Rydt, J., Jenkins, A., Holland, P. R., Ha, H. K., Lee, S. H., Steig, E. J., Ding, Q., Abrahamsen, E. P., and Schroder, M.: Strong Sensitivity of Pine Island Ice-Shelf Melting to Climatic Variability, Science, 343, 174–178, https://doi.org/10.1126/science.1244341, 2014.

Epstein, S. and Mayeda, T.: Variation of 18O content of waters from natural sources, Geochem. Cosmochem. Acta, 4, 213–224, 1953.

Flexas, M. M., Thompson, A., Schodlok, M., Zhang, H., and Speer, K.: Antarctic Peninsula warming triggers enhanced basal melt rates throughout West Antarctica, Sci. Adv., 12, 2022.

Fogwill, C. J., Phipps, S. J., Turney, C. S. M., and Golledge, N. R.: Sensitivity of the Southern Ocean to enhanced regional Antarctic ice sheet meltwater input, Earths Future, 3, 317–329, https://doi.org/10.1002/2015EF000306, 2015.

Fretwell, P., Pritchard, H. D., Vaughan, D. G., Bamber, J. L., Barrand, N. E., Bell, R., Bianchi, C., Bingham, R. G., Blankenship, D. D., Casassa, G., Catania, G., Callens, D., Conway, H., Cook, A. J., Corr, H. F. J., Damaske, D., Damm, V., Ferraccioli, F., Forsberg, R., Fujita, S., Gim, Y., Gogineni, P., Griggs, J. A., Hindmarsh, R. C. A., Holmlund, P., Holt, J. W., Jacobel, R. W., Jenkins, A., Jokat, W., Jordan, T., King, E. C., Kohler, J., Krabill, W., Riger-Kusk, M., Langley, K. A., Leitchenkov, G., Leuschen, C., Luyendyk, B. P., Matsuoka, K., Mouginot, J., Nitsche, F. O., Nogi, Y., Nost, O. A., Popov, S. V., Rignot, E., Rippin, D. M., Rivera, A., Roberts, J., Ross, N., Siegert, M. J., Smith, A. M., Steinhage, D., Studinger, M., Sun, B., Tinto, B. K., Welch, B. C., Wilson, D., Young, D. A., Xiangbin, C., and Zirizzotti, A.: Bedmap2: improved ice bed, surface and thickness datasets for Antarctica, The Cryosphere, 7, 375–393, https://doi.org/10.5194/tc-7-375-2013, 2013.

Friedman, I. and Smith, G. I.: Deuterium Content of Snow Cores from Sierra Nevada Area, Science, 169, 467–470, https://doi.org/10.1126/science.169.3944.467, 1970.

Gat, J. R. and Gonfiantini, R.: Stable isotope hydrology: deuterium and oxygen-18 in the water cycle. Technical reports series No. 210, 1981.

Global Network of Isotopes in Precipitation (GNIP): Water Isotope System for data analysis, visualizaiton and Electronic Retrieval (WISER), IAEA, 2023.

Hellmer, H. H., Jacobs, S. S., and Jenkins, A.: Oceanic Erosion of a Floating Antarctic Glacier in the Amundsen Sea, in: Ocean, Ice, and Atmosphere: Interactions at the Antarctic Continental Margin, vol. 75, edited by: Jacobs, S. S. and Weiss, R. F., American Geophysical Union, Washington, D. C., 83–99, https://doi.org/10.1029/AR075p0083, 1998.

Holland, P. R., Bracegirdle, T. J., Dutrieux, P., Jenkins, A., and Steig, E. J.: West Antarctic ice loss influenced by internal climate variability and anthropogenic forcing, Nat. Geosci., 12, 718–724, https://doi.org/10.1038/s41561-019-0420-9, 2019.

Ingraham, N. L.: Chapter 3 - Isotopic Variations in Precipitation, in: Isotope Tracers in Catchment Hydrology, edited by: Kendall, C. and McDONNELL, J. J., Elsevier, Amsterdam, 87–118, https://doi.org/10.1016/B978-0-444-81546-0.50010-0, 1998.

IPCC: The Ocean and Cryosphere in a Changing Climate: Special Report of the Intergovernmental Panel on Climate Change, 1st ed., Cambridge University Press, https://doi.org/10.1017/9781009157964, 2022.

Jacobs, S. S., Fairbanks, R. G., and Horibe, Y.: Origin and evolution of water masses near the Antarctic continental margin: Evidence from H2 18O / H2 16O ratios in seawater, Oceanol. Antarct. Cont. Shelf, 43, 59–85, https://doi.org/10.1029/AR043, 1985.

Jacobs, S. S., Hellmer, H. H., and Jenkins, A.: Antarctic Ice Sheet melting in the southeast Pacific, Geophys. Res. Lett., 23, 957–960, https://doi.org/10.1029/96GL00723, 1996.

Jacobs, S. S., Giulivi, C. F., and Mele, P. A.: Freshening of the Ross Sea during the late 20th century., Science, 297, 386–389, https://doi.org/10.1126/science.1069574, 2002.

Jacobs, S. S., Jenkins, A., Giulivi, C. F., and Dutrieux, P.: Stronger ocean circulation and increased melting under Pine Island Glacier ice shelf, Nat. Geosci., 4, 519–523, https://doi.org/10.1038/ngeo1188, 2011.

Jenkins, A., Dutrieux, P., Jacobs, S. S., McPhail, S. D., Perrett, J. R., Webb, A. T., and White, D.: Observations beneath Pine Island Glacier in West Antarctica and implications for its retreat, Nat. Geosci., 3, 468–472, https://doi.org/10.1038/ngeo890, 2010.

Jenkins, A., Shoosmith, D., Dutrieux, P., Jacobs, S. S., Kim, T. W., Lee, S. H., Ha, H. K., and Stammerjohn, S.: West Antarctic Ice Sheet retreat in the Amundsen Sea driven by decadal oceanic variability, Nat. Geosci., 11, 733–738, https://doi.org/10.1038/s41561-018-0207-4, 2018.

Jeon, M. H., Jung, J., Park, M. O., Aoki, S., Kim, T.-W., and Kim, S.-K.: Tracing Circumpolar Deep Water and glacial meltwater using humic-like fluorescent dissolved organic matter in the Amundsen Sea, Antarctica, Mar. Chem., 235, 104008, https://doi.org/10.1016/j.marchem.2021.104008, 2021.

Joughin, I., Tulaczyk, S., Bamber, J. L., Blankenship, D., Holt, J. W., Scambos, T., and Vaughan, D. G.: Basal conditions for Pine Island and Thwaites Glaciers, West Antarctica, determined using satellite and airborne data, J. Glaciol., 55, 245–257, https://doi.org/10.3189/002214309788608705, 2009.

Joughin, I., Shapero, D., Smith, B., Dutrieux, P., and Barham, M.: Ice-shelf retreat drives recent Pine Island Glacier speedup, Sci. Adv., 7, eabg3080, https://doi.org/10.1126/sciadv.abg3080, 2021.

Kim, T.-W., Yang, H. W., Dutrieux, P., Wåhlin, A. K., Jenkins, A., Kim, Y. G., Ha, H. K., Kim, C.-S., Cho, K.-H., Park, T., Park, J., Lee, S., and Cho, Y. K.: Interannual Variation of Modified Circumpolar Deep Water in the Dotson-Getz Trough, West Antarctica, J. Geophys. Res. Oceans, n/a, e2021JC017491, https://doi.org/10.1029/2021JC017491, 2021.

Kimura, S., Jenkins, A., Regan, H., Holland, P. R., Assmann, K. M., Whitt, D. B., Van Wessem, M., van de Berg, W. J., Reijmer, C. H., and Dutrieux, P.: Oceanographic Controls on the Variability of Ice-Shelf Basal Melting and Circulation of Glacial Meltwater in the Amundsen Sea Embayment, Antarctica, J. Geophys. Res. Oceans, 122, 10131–10155, https://doi.org/10.1002/2017JC012926, 2017.

Leclerc, A. J. and Labeyrie, L.: Temperature dependence of the oxygen isotopic fractionation between diatom silica and water, Earth Planet. Sci. Lett., 84, 69–74, https://doi.org/10.1016/0012-821X(87)90177-4, 1987.

Lécuyer, C., Gardien, V., Rigaudier, T., Fourel, F., Martineau, F., and Cros, A.: Oxygen isotope fractionation and equilibration kinetics between CO2 and H2O as a function of salinity of aqueous solutions, Chem. Geol., 264, 122–126, https://doi.org/10.1016/j.chemgeo.2009.02.017, 2009.

van der Linden, E. C., Le Bars, D., Lambert, E., and Drijfhout, S.: Calibration of basal melt on past ice discharge lowers projections of Antarctica's sea level contribution, Ice sheets/Antarctic, https://doi.org/10.5194/tc-2021-348, 2021.

van der Linden, E. C., Le Bars, D., Lambert, E., and Drijfhout, S.: Antarctic contribution to future sea level from ice shelf basal melt as constrained by ice discharge observations, The Cryosphere, 17, 79–103, https://doi.org/10.5194/tc-17-79-2023, 2023.

Mallett, H. K. W., Boehme, L., Fedak, M., Heywood, K. J., Stevens, D. P., and Roquet, F.: Variation in the Distribution and Properties of Circumpolar Deep Water in the Eastern Amundsen Sea, on Seasonal Timescales, Using Seal-Borne Tags, Geophys. Res. Lett., 45, 4982–4990, https://doi.org/10.1029/2018GL077430, 2018.

Mankoff, K. D., Jacobs, S. S., Tulaczyk, S. M., and Stammerjohn, S. E.: The role of Pine Island Glacier ice shelf basal channels in deep-water upwelling, polynyas and ocean circulation in Pine Island Bay, Antarctica, Ann. Glaciol., 53, 123–128, https://doi.org/10.3189/2012AoG60A062, 2012.

Masson-Delmotte, V., Hou, S., Ekaykin, A., Jouzel, J., Aristarain, A., Bernardo, R. T., Bromwich, D., Cattani, O., Delmotte, M., Falourd, S., Frezzotti, M., Gallée, H., Genoni, L., Isaksson, E., Landais, A., Helsen, M. M., Hoffmann, G., Lopez, J., Morgan, V., Motoyama, H., Noone, D., Oerter, H., Petit, J. R., Royer, A., Uemura, R., Schmidt, G. A., Schlosser, E., Simões, J. C., Steig, E. J., Stenni, B., Stievenard, M., van den Broeke, M. R., van de Wal, R. S. W., van de Berg, W. J., Vimeux, F., and White, J. W. C.: A Review of Antarctic Surface Snow Isotopic Composition: Observations, Atmospheric Circulation, and Isotopic Modeling*, J. Clim., 21, 3359–3387, https://doi.org/10.1175/2007JCLI2139.1, 2008.

Meredith, M. P., Brandon, M. A., Wallace, M. I., Clarke, A., Leng, M. J., Renfrew, I. A., van Lipzig, N. P. M., and King, J. C.: Variability in the freshwater balance of northern Marguerite Bay, Antarctic Peninsula: Results from δ18O, Deep-Sea Res. II, 55, 309–322, https://doi.org/10.1016/j.dsr2.2007.11.005, 2008.

Meredith, M. P., Wallace, M. I., Stammerjohn, S. E., Renfrew, I. A., Clarke, A., Venables, H. J., Shoosmith, D. R., Souster, T., and Leng, M. J.: Changes in the freshwater composition of the upper ocean west of the Antarctic Peninsula during the first decade of the 21st century, Prog. Oceanogr., 87, 127–143, https://doi.org/10.1016/j.pocean.2010.09.019, 2010.

Meredith, M. P., Venables, H. J., Clarke, A., Ducklow, H. W., Erickson, M., Leng, M. J., Lenaerts, J. T. M., and van den Broeke, M. R.: The Freshwater System West of the Antarctic Peninsula: Spatial and Temporal Changes, J. Clim., 26, 1669–1684, https://doi.org/10.1175/JCLI-D-12-00246.1, 2013.

Meredith, M. P., Falk, U., Bers, A. V., Mackensen, A., Schloss, I. R., Ruiz Barlett, E., Jerosch, K., Silva Busso, A., and Abele, D.: Anatomy of a glacial meltwater discharge event in an Antarctic cove, Philos. Trans. R. Soc. Math. Phys. Eng. Sci., 376, 20170163, https://doi.org/10.1098/rsta.2017.0163, 2018.

Mosley-Thompson, E., Thompson, L. G., Grootes, P. M., and Gundestrup, N.: Little Ice Age (Neoglacial) Paleoenvironmental Conditions At Siple Station, Antarctica, Ann. Glaciol., 14, 199–204, https://doi.org/10.3189/S0260305500008570, 1990.

Nakayama, Y., Schröder, M., and Hellmer, H. H.: From circumpolar deep water to the glacial meltwater plume on the eastern Amundsen Shelf, Deep Sea Res. Part Oceanogr. Res. Pap., 77, 50–62, https://doi.org/10.1016/j.dsr.2013.04.001, 2013.

Nakayama, Y., Manucharyan, G., Zhang, H., Dutrieux, P., Torres, H. S., Klein, P., Seroussi, H., Schodlok, M., Rignot, E., and Menemenlis, D.: Pathways of ocean heat towards Pine Island and Thwaites grounding lines, Sci. Rep., 9, 16649, https://doi.org/10.1038/s41598-019-53190-6, 2019.

Naveira Garabato, A. C. N., Forryan, A., Dutrieux, P., Brannigan, L., Biddle, L. C., Heywood, K. J., Jenkins, A., Firing, Y. L., and Kimura, S.: Vigorous lateral export of the meltwater outflow from beneath an Antarctic ice shelf, Nature, 542, 219–222, https://doi.org/10.1038/nature20825, 2017.

Noone, D. and Simmonds, I.: Annular variations in moisture transport mechanisms and the abundance of δ18O in Antarctic snow, J. Geophys. Res. Atmospheres, 107, ACL 3-1-ACL 3-11, https://doi.org/10.1029/2002JD002262, 2002.

Östlund, H. G. and Hut, G.: Arctic Ocean water mass balance from isotope data, J. Geophys. Res. Oceans, 89, 6373–6381, https://doi.org/10.1029/JC089iC04p06373, 1984.

Paolo, F. S., Fricker, H. A., and Padman, L.: Volume loss from Antarctic ice shelves is accelerating, Science, 348, 327–331, https://doi.org/10.1126/science.aaa0940, 2015.

Paolo, F. S., Padman, L., Fricker, H. A., Adusumilli, S., Howard, S., and Siegfried, M. R.: Response of Pacific-sector Antarctic ice shelves to the El Niño/Southern Oscillation, Nat. Geosci., 11, 121–126, https://doi.org/10.1038/s41561-017-0033-0, 2018.

Pritchard, H. D., Ligtenberg, S. R. M., Fricker, H. A., Vaughan, D. G., van den Broeke, M. R., and Padman, L.: Antarctic ice-sheet loss driven by basal melting of ice shelves, Nature, 484, 502–505, https://doi.org/10.1038/nature10968, 2012.

Randall-Goodwin, E., Meredith, M. P., Jenkins, A., Yager, P. L., Sherrell, R. M., Abrahamsen, E. P., Guerrero, R., Yuan, X., Mortlock, R. A., Gavahan, K., Alderkamp, A.-C., Ducklow, H., Robertson, R., and Stammerjohn, S. E.: Freshwater distributions and water mass structure in the Amundsen Sea Polynya region, Antarctica, Elem. Sci. Anthr., 3, 000065, https://doi.org/10.12952/journal.elementa.000065, 2015.

Rignot, E. and Jacobs, S. S.: Rapid Bottom Melting Widespread near Antarctic Ice Sheet Grounding Lines, Science, 296, 2020–2023, https://doi.org/10.1126/science.1070942, 2002.

Rignot, E., Velicogna, I., Van Den Broeke, M. R., Monaghan, A., and Lenaerts, J.: Acceleration of the contribution of the Greenland and Antarctic ice sheets to sea level rise, Geophys. Res. Lett., 38, 1–5, https://doi.org/10.1029/2011GL046583, 2011.

Rignot, E., Jacobs, S. S., Mouginot, J., and Scheuchl, B.: Ice-Shelf Melting Around Antarctica, Science, 341, 266–270, https://doi.org/10.1126/science.1235798, 2013.

Rignot, E., Mouginot, J., Scheuchl, B., van den Broeke, M., van Wessem, M. J., and Morlighem, M.: Four decades of Antarctic Ice Sheet mass balance from 1979–2017, Proc. Natl. Acad. Sci., 116, 1095–1103, https://doi.org/10.1073/pnas.1812883116, 2019a.

Rignot, E., Mouginot, J., Scheuchl, B., van den Broeke, M., van Wessem, M. J., and Morlighem, M.: Four decades of Antarctic Ice Sheet mass balance from 1979–2017, Proc. Natl. Acad. Sci., 116, 1095–1103, https://doi.org/10.1073/pnas.1812883116, 2019b.

Rohling, E. J.: PALEOCEANOGRAPHY, PHYSICAL AND CHEMICAL PROXIES | Oxygen Isotope Composition of Seawater, in: Encyclopedia of Quaternary Science, Elsevier, 915–922, https://doi.org/10.1016/B978-0-444-53643-3.00293-4, 2013.

Rubin, S. I., Takahashi, T., Chipman, D. W., and Goddard, J. G.: Primary productivity and nutrient utilization ratios in the Pacific sector of the Southern Ocean based on seasonal changes in seawater chemistry, Deep Sea Res. Part Oceanogr. Res. Pap., 45, 1211–1234, https://doi.org/10.1016/S0967-0637(98)00021-1, 1998.

Sato, T. and Nakamura, T.: Altitude effects of hydrogen and oxygen isotopic ratios of precipitation in the northern part of Awaji Island, Japan, J. Jpn. Assoc. Hydrol. Sci., 35, 15–22, https://doi.org/10.4145/jahs.35.15, 2005.

Schaffer, J., Timmermann, R., Arndt, J. E., Steinhage, D., and Kanzow, T.: RTopo-2: A global dataset of ice sheet topography, cavity geometry and ocean bathymetry to study ice-ocean interaction in Northeast Greenland, in: EPIC3REKLIM conference “Our Climate - Our Future”, Berlin, Germany, 2014-10-06-2014-10-09, REKLIM conference “Our Climate - Our Future,” Berlin, Germany, 2014.

Schneider, D. P., Steig, E. J., van Ommen, T. D., Dixon, D. A., Mayewski, P. A., Jones, J. M., and Bitz, C. M.: Antarctic temperatures over the past two centuries from ice cores, Geophys. Res. Lett., 33, https://doi.org/10.1029/2006GL027057, 2006.

Shepherd, A., Gilbert, L., Muir, A. S., Konrad, H., McMillan, M., Slater, T., Briggs, K. H., Sundal, A. V., Hogg, A. E., and Engdahl, M. E.: Trends in Antarctic Ice Sheet Elevation and Mass, Geophys. Res. Lett., 46, 8174–8183, https://doi.org/10.1029/2019GL082182, 2019.

Siegenthaler, U. and Oeschger, H.: Correlation of 18O in precipitation with temperature and altitude, Nature, 285, 314–317, https://doi.org/10.1038/285314a0, 1980.

Silvano, A., Rintoul, S. R., Peña-Molino, B., Hobbs, W. R., Wijk, E. van, Aoki, S., Tamura, T., and Williams, G. D.: Freshening by glacial meltwater enhances melting of ice shelves and reduces formation of Antarctic Bottom Water, Sci. Adv., 4, eaap9467, https://doi.org/10.1126/sciadv.aap9467, 2018.

Skrzypek, G. and Ford, D.: Stable Isotope Analysis of Saline Water Samples on a Cavity Ring-down Spectroscopy Instrument, Environ. Sci. Technol., 48, 2827–2834, https://doi.org/10.1021/es4049412, 2014.

Steig, E. J., Mayewski, P. A., Dixon, D. A., Kaspari, S. D., Frey, M. M., Schneider, D. P., Arcone, S. A., Hamilton, G. S., Blue Spikes, V., Mary Albert, Meese, D., Gow, A. J., Shuman, C. A., White, J. W. C., Sneed, S., Flaherty, J., and Wumkes, M.: High-resolution ice cores from US ITASE (West Antarctica): development and validation of chronologies and determination of precision and accuracy, Ann. Glaciol., 41, 77–84, https://doi.org/10.3189/172756405781813311, 2005.

Tamsitt, V., England, M. H., Rintoul, S. R., and Morrison, A. K.: Residence Time and Transformation of Warm Circumpolar Deep Water on the Antarctic Continental Shelf, Geophys. Res. Lett., 48, https://doi.org/10.1029/2021GL096092, 2021.

Thomas, E. R., Dennis, P. F., Bracegirdle, T. J., and Franzke, C.: Ice core evidence for significant 100-year regional warming on the Antarctic Peninsula, Geophys. Res. Lett., 36, https://doi.org/10.1029/2009GL040104, 2009.

Thurnherr, A. M., Jacobs, S. S., Dutrieux, P., and Giulivi, C. F.: Export and circulation of ice cavity water in Pine Island Bay, West Antarctica, J. Geophys. Res. Oceans, 119, 1754–1764, https://doi.org/10.1002/2013JC009307, 2014.

Velicogna, I., Sutterley, T. C., and Broeke, M. R. van den: Regional acceleration in ice mass loss from Greenland and Antarctica using GRACE time-variable gravity data, Geophys. Res. Lett., 41, 8130–8137, https://doi.org/10.1002/2014GL061052, 2014.

Wåhlin, A. K., Graham, A. G. C., Hogan, K. A., Queste, B. Y., Boehme, L., Larter, R. D., Pettit, E. C., Wellner, J., and Heywood, K. J.: Pathways and modification of warm water flowing beneath Thwaites Ice Shelf, West Antarctica, Sci. Adv., 7, eabd7254, https://doi.org/10.1126/sciadv.abd7254, 2021.

Walker, S. A., Azetsu-Scott, K., Normandeau, C., Kelley, D. E., Friedrich, R., Newton, R., Schlosser, P., McKay, J. L., Abdi, W., Kerrigan, E., Craig, S. E., and Wallace, D. W. R.: Oxygen isotope measurements of seawater (H2 18O/H2 16O): A comparison of cavity ring-down spectroscopy (CRDS) and isotope ratio mass spectrometry (IRMS), Limnol. Oceanogr. Methods, 14, 31–38, https://doi.org/10.1002/lom3.10067, 2016.

WCRP Global Sea Level Budget Group: Global sea-level budget 1993–present, Earth Syst. Sci. Data, 10, 1551–1590, https://doi.org/10.5194/essd-10-1551-2018, 2018.